Intrinsic timescales as an organizational principle of neural processing across the whole rhesus macaque brain

Ana M.G. Manea[1,2]†, Anna Zilverstand[3,4], Kâmil Uğurbil[2,5,6], Sarah R. Heilbronner[1,4,5], Jan Zimmermann[1,2,4,5,7]

Affiliation

1. Department of Neuroscience
2. Center for Magnetic Resonance Research
3. Department of Psychiatry & Behavioral Sciences
4. Medical Discovery Team on Addiction
5. Center for Neuroengineering
6. Department of Radiology
7. Department of Biomedical Engineering

University of Minnesota, Minneapolis MN 55455

† **Corresponding author**

Ana Manea
Department of Neuroscience,
Center for Magnetic Resonance Research
University of Minnesota
Minneapolis, MN, 55455
Email:manea006@umn.edu

Keywords

Functional connectivity, rhesus macaque, resting-state, spontaneous activity, functional MRI (fMRI), gradients, timescales, ultrahigh field, 10.5 Tesla

Acknowledgements

We thank Steve Jungst, Gregor Adriany and Russell Lagore for continuing support with our coils and hardware. We thank Jen Holmberg, Brenna Knaebe and Mrunal Zambre, for support with animal care and data acquisition.

Funding statement

This work was supported by NIH grants P41 EB027061 (to JZ, KU), R01 MH118257 (to SRH), R56 EB031765 (to JZ), R01 MH128177 (to JZ), from the Digital Technologies Initiative (to JZ), from the Minnesota Institute of Robotics (to JZ), two Young Investigator Awards from the Brain & Behavior Research Foundation to SRH and AZ, a P30DA048742 (to JZ, SRH, and AZ), and a UMN AIRP award to JZ, SRH and AZ.

Abstract

Hierarchical temporal dynamics are a fundamental computational property of the brain; however, there are no whole-brain, noninvasive investigations into timescales of neural processing in animal models. To that end, we used the spatial resolution and sensitivity of ultrahigh field fMRI performed at 10.5 Tesla to probe timescales across the whole macaque brain. We uncovered within-species consistency between timescales estimated from fMRI and electrophysiology. Crucially, we extended existing electrophysiological hierarchies to whole brain topographies. Our results validate the complementary use of hemodynamic and electrophysiological intrinsic timescales, establishing a basis for future translational work. Further, with these results in hand, we were able to show that one facet of the high-dimensional functional connectivity topography of any region in the brain is closely related to hierarchical temporal dynamics. We demonstrated that intrinsic timescales are organized along spatial gradients that closely match functional connectivity gradient topographies across the whole brain. We conclude that intrinsic timescales are a unifying organizational principle of neural processing across the whole brain.

Declaration of Interests

The authors declare no competing interests.

1. Introduction

Recent work supports the idea that the neural processing is organized over multiple timescales (Cavanagh, Hunt, & Kennerley, 2020; Hasson, Yang, Vallines, Heeger, & Rubin, 2008; Honey et al., 2012; Kiebel, Daunizeau, & Friston, 2008; Murray et al., 2014; Raut, Snyder, & Raichle, 2020; Soltani, Murray, Seo, & Lee, 2021). Hierarchical temporal dynamics are a fundamental computational property of the brain—fast changing sensory input is encoded by the fast dynamics of sensory areas, which is in turn integrated into temporally extended representations encoded by the slower dynamics of higher-order areas (Cavanagh et al., 2020; Raut et al., 2020; Soltani et al., 2021). Temporal integration and information processing over multiple timescales are crucial for understanding how the brain deals with the complexity of the real world (Zimmermann, Glimcher, & Louie, 2018), hence, understanding whole brain temporal dynamics is highly important.

As one moves from sensory to associative areas, neural processing reflects a hierarchy of progressively longer "temporal receptive windows" (TRW)—defined as the length of time during which an area accumulates information during task performance (Hasson et al., 2008). In other words, the range of the TRW of each area reflects its functional role, with sensory areas having short TRWs, to enable fast sensory processing, and associative areas having longer TRWs, allowing them to process information unfolding over longer periods of time. Not only does neural processing display these timescales during task performance, but we now know that temporal specialization arises from a region's intrinsic dynamics, that is, temporal dynamics that are present even in the absence of direct sensory stimulation. This was first described by Murray and colleagues (2014) analyzing action potentials of single neurons in the macaque. They showed that timescales of baseline neuronal activity vary across cortical areas, revealing a hierarchical progression from fast timescales in sensory areas, to slower timescales in association areas. These intrinsic fluctuations in the neural signal, also described as intrinsic neural timescales (INTs), are thought to set the duration over which brain regions integrate inputs (Murray et al., 2014). They are hypothesized to be the result of multiple neuronal mechanisms, including local dynamics and recurrent connectivity (Murray et al., 2014; Soltani et al., 2021; Watanabe, Rees, & Masuda, 2019).

Additional studies have replicated and extended the INT hierarchy, reinforcing the idea that brain regions exhibit unique timescales in their intrinsic activity, which reflect functional specialization in terms of temporal integration (Cavanagh, Wallis, Kennerley, & Hunt, 2016;

Cirillo, Fascianelli, Ferrucci, & Genovesio, 2018; Fascianelli, Tsujimoto, Marcos, & Genovesio, 2019; Murray et al., 2014; Ogawa & Komatsu, 2010; Rossi-Pool et al., 2021, Maisson et al., 2021). The concept of INT hierarchy has even been extended to subcortical regions—specifically the basal ganglia (Nougaret, Fascianelli, Ravel, & Genovesio, 2021). Moreover, a large-scale network model, based on anatomical connectivity and the strength of local recurrent connectivity, has been used to successfully reproduce the temporal hierarchy (Chaudhuri, Knoblauch, Gariel, Kennedy, & Wang, 2015). This suggests that anatomical connectivity is closely related to INTs.

Alterations in hierarchical INT patterns can result in cognitive and behavioral abnormalities (Watanabe et al., 2019; Wengler, Goldberg, Chahine, & Horga, 2020; Zilio et al., 2021). For example, abnormal INT patterns have been associated with core symptoms of high-functioning individuals with Autism Spectrum Disorder (Watanabe et al., 2019). Likewise, delusions and hallucinations are associated with INT alterations at different hierarchical levels, leading to symptom-specific changes in hierarchical INT gradients (Wengler et al., 2020). Hence, investigations into INTs have the potential to clarify hierarchical dysfunction in whole-brain dynamics in neuropsychiatric disorders.

Traditionally, INTs have been investigated using invasive electrophysiology, which is not suited to uncover whole-brain dynamics. It is also challenging to collect in humans, particularly for large datasets (as would be needed to assess differences across populations). One way to overcome this problem is using functional magnetic resonance imaging (fMRI), which offers whole brain coverage and can be performed across species and in larger sample sizes. However, it is not yet clear whether hemodynamic INTs derived from fMRI reflect similar neural phenomena as those derived from electrophysiology. To clarify this issue, electrophysiological and hemodynamic INTs must be compared directly within the same species. To that end, recent advancements in non-human primate (NHP) neuroimaging, based on the use of very high magnetic fields (10.5T) for significantly boosting signal-to-noise ratios (SNR) (Lagore et al., 2021; Yacoub et al., 2020), make it possible to study hemodynamic INTs in the macaque brain. Moreover, taking advantage of the whole-brain coverage of fMRI, we are investigating INT topography. This is important since more recent work has shown that there is significant heterogeneity within regions (Cavanagh et al., 2020; Cirillo et al., 2018; Nougaret et al., 2021), even though initially INTs were assigned to cortical regions as a whole,

In addition to INTs, gradients of functional connectivity (FC) can also describe the functional architecture of neural processing (Haak, Marquand, & Beckmann, 2018; Vos de Wael et al., 2020). Gradient approaches map macroscale brain features to low dimensional manifold representations (Vos de Wael et al., 2020). Gradient mapping has the potential to uncover overlapping functional topographies by treating the high dimensional connectivity structure as a spatial variance decomposition problem. Notably, this approach finds patterns in the high-dimensional FC similarity structure that describe the spatial direction of maximum FC variance. For example, areas in the early visual cortex are known to exhibit at least two gradual modes of functional change (i.e., eccentricity and polar angle maps), which can be successfully retrieved from resting-state FC via gradient mapping (Haak et al., 2018). The existence of multiple overlapping principles of topographic organization is likely a general property of the whole brain (Haak et al., 2018; Harvey, Dumoulin, Fracasso, & Paul, 2020; Jbabdi, Sotiropoulos, & Behrens, 2013; Marquand, Haak, & Beckmann, 2017; Przeździk, Faber, Fernández, Beckmann, & Haak, 2019). Here, we carry out an investigation into the multi-dimensional functional architecture of the macaque brain by probing its spatial and temporal intrinsic dynamics. This allows us to achieve several significant goals. First, we are able to relate fMRI hemodynamic timescales to the gold standards of electrophysiology within the same species. Second, with these results in hand, we are able to show that one facet of the high-dimensional FC topography of any region in the brain is closely related to INT topography. We show that the hierarchical intrinsic dynamics of neural processing manifest into gradients of INTs and FC which follow the same gradual topographical arrangement. In sum, we reliably describe one facet of the macroscale functional organization of the brain, with respect to spatial and temporal dynamics.

2. Results

2.1. INT hierarchies

First, we set out to replicate and validate findings from electrophysiological INT estimation with ultrahigh field fMRI. Murray and colleagues (2014) initially described (in macaques) a visual cortical hierarchy of seven cortical areas: middle temporal area (MT), lateral intraparietal (LIP) area, orbitofrontal cortex (OFC), lateral PFC (LPFC), anterior cingulate cortex (ACC); and a somatosensory hierarchy including primary somatosensory (S1) and secondary somatosensory (S2) cortex (Figure 1A-B Left). This cortical hierarchy has been replicated and further extended by assigning INTs to the dorsal premotor (PMd) cortex, frontopolar cortex (PFp), ventral and

dorsal LPFC (VLPFC, DLPFC) (Cavanagh et al., 2016; Cirillo et al., 2018; Fascianelli et al., 2019) (Figure 1C-D Left). Recently, INTs have been estimated in the medial wall of the PFC, including the ventromedial PFC (vmPFC), subgenual ACC (sgACC), pregenual ACC (pgACC), and dorsal ACC (dACC) (Maisson et al., 2021) (Figure 1E Left). Lastly, a subcortical INT hierarchy has been described for regions of the basal ganglia: external segment of the globus pallidus (GPe), subthalamic nucleus (STN), and the striatum (Nougaret et al., 2021) (Figure 1F Left).

The electrophysiology-based (Figure 1 Left) and fMRI-based (Figure 1 Right) INTs reveal similar hierarchies across the brain. By replicating these physiological hierarchies, we demonstrate that fMRI is well-suited to investigate aspects of whole-brain temporal dynamics. Minor deviations from hierarchies estimated from single-unit recordings (e.g., in STN, sgACC, pgACC) can be attributed to several factors such as a high degree of INT heterogeneity within these regions, and differences between studies in the atlases used and size of the areas under investigation (see Figure 1 Supplement 3 for the INT stability analysis).

Our definition of INTs combines the effects of ACF magnitude and timescale (i.e., the 0-crossing lag). Since it has previously been shown that the magnitude of the ACF values, parameterized as the lag-1 ACF value, differs across brain areas (Shinn et al., 2021), we further examined whether the observed hierarchies are driven by magnitude, timescale, or both. In line with previous results, the lag-1 ACF values systematically varied across the brain (Shinn et al., 2021). Moreover, the lag-1 ACF values and the 0-crossing lag were linearly related to INTs as operationalized in this study (see Figure 1 Supplement 1 for voxel-wise whole-brain maps of the lag-1, 0-crossing lag, and INTs). The maps suggest that magnitude and timescale are closely related. To exclude the possibility that the observed hierarchies are driven by magnitude, rather than timescale, we re-computed them by using the 0-crossing lag as a proxy for INT. To obtain a time estimate of hemodynamic timescales, the 0-lag crossing lag was multiplied by the TR (i.e., 1.1s). The hierarchical ordering of both cortical and subcortical areas is consistent (see Figure 1 Supplement 2) with that based on our INT measure (see Figure 1). Hence, while the ACF magnitude is closely related to our INT index and the 0-crossing lag, temporal hierarchies are not driven by heterogeneity in the ACF magnitude.

We next investigated previously unexamined regions, making unique use of our high resolution, whole-brain coverage. Specifically, we reveal a hierarchy of INTs in the dorsal visual pathway (Goodale et al., 1994; Goodale & Milner, 1992) (Figure 2). INTs gradually increase from

the entry point of visual information to higher order areas involved in visuo-motor integration (Figure 2, inset). INTs are hierarchically organized within the occipito-parietal, parieto-premotor and parieto-prefrontal components of the dorsal pathway (Kravitz, Saleem, Baker, & Mishkin, 2011). Also, in line with the occipito-parietal pathway being the source of the other two pathways, it is lower in the hierarchy. Taken together, we replicate electrophysiological INT hierarchies and demonstrate the invaluable contribution of using whole-brain fMRI to extend this research by describing a previously uncharacterized fine-grained temporal hierarchy along the visual pathway as an example.

2.2. INT hierarchies are closely related to FC gradients across the brain

We next examined the relationship between INTs and gradients of FC at different levels of description, starting with the frontal and parietal lobes (see Figure 3, gradients computed twice, once using within-lobe FC and again using frontal-parietal FC). In the frontal lobe, the first component (i.e., G1) shows an overall anterior-posterior organization spanning from sensory to motor areas. This aligns with previous studies showing a global anterior-posterior functional gradient in the frontal lobe (Badre, 2008; Riley, Qi, Zhou, & Constantinidis, 2018; Tan, Tang, Herikstad, Pillay, & Libedinsky, 2020). The second component (i.e., G2) shows an overall lateral-medial organization, extending from the PMv to the medial wall. The INT map was correlated with G2 for both within-area ($r = 0.47$) and fronto-parietal ($r = -0.26$) connectivity. In the parietal lobe, G1 showed a medial-lateral and G2 a ventro-dorsal overall organization. The INT map was correlated with G1 for both within-area ($r = 0.56$) and fronto-parietal ($r = 0.47$) connectivity. (Note that the sign of the gradients is arbitrary as a byproduct of the decomposition method (Haak & Beckmann, 2020), hence, only the magnitude but not the direction of the INT-FC gradient correlation is relevant.)

We then selected functionally meaningful subdivisions of the frontal lobe to probe finer-grained connectivity profiles and interrogate the existence of multiple hierarchical gradients of function (see Figure 4). In all cases, the INT maps were highly correlated with one of the principal components estimated from within-area connectivity (i.e., LPFC G1: $r = 0.35$; Motor G1: $r = 0.68$; OFC G2: $r = 0.45$; MPFC G1: $r = 0.49$). For example, the motor cortex has a well-established hierarchy, with premotor regions at the top and M1 at the bottom (Binkofski & Buxbaum, 2013; Wong, Haith, & Krakauer, 2015). Accordingly, the maps reflected this functional hierarchy, with M1 being at one end and the PMv at the other. The OFC shows a predominantly anterior-posterior

axis of change, which agrees with anatomical findings—the caudal and lateral regions are more input-like unimodal regions while more anterior areas integrate these multi-modal signals (Carmichael & Price, 1994, 1996; Öngür & Price, 2000; Price, 1999). The lateral and medial subdivisions of the PFC revealed a predominately anterior-posterior organization. The same pattern of results was observed at the single-subject level (see Figure 4 Supplement 2).

Although we were mainly interested in the fine-grained functional organization of individual areas, we also asked whether the INT-FC relationship holds at the whole-cortex level (see Figure 3 Supplement 1). It is important to note that the whole-cortex estimation reflects overall inter-areal FC differences rather than the fine-grained FC patterns in smaller areas; that is because inter-areal connectivity differences are more pronounced than intra-areal differences. The whole-cortex INT map was highly correlated with the second gradient estimated from the cortical FC matrix ($r = 0.70$). With these results in hand, we conclude that INTs and FC gradients are closely related and represent a functional principle of organization across the whole brain.

We then investigated cortical-subcortical hierarchical gradients of function. Cortico-striatal anatomical connectivity has been extensively studied in NHPs, however, striatal-cortical FC and INTs have not. The striatal INT map was correlated with the FC gradient estimated from cortico-striatal ($r= 0.38$) connectivity (see Figure 5). The cortico-striatal FC topography exhibited a gradual pattern of connectivity change corresponding to the anterior-posterior, dorsal-ventral, and medial-lateral anatomical gradient of connectivity derived from tract-tracing studies in NHPs (Haber et al., 2006; Friedman et al., 2002; Alexander et al., 1986; Cho et al., 2013). INTs followed a similar pattern. Moreover, the FC gradients were similar to those estimated from human neuroimaging data (Marquand, Haak, & Beckmann, 2017). To examine the underlying FC patterns, we projected the striatal gradient onto the cortex (see Figure 5A). This analysis not only validated the meaning of the gradients, but also revealed that the cortico-striatal FC closely matched anatomical connectivity. To further investigate the link between FC and INTs, we reconstructed the striatal INT map by replacing the INT of every voxel with the average INT value of the cortical voxels (i.e., 10 voxels) with which they are most correlated (see Figure 5B). In accordance with the above-mentioned results, the striatal INTs and reconstructed cortico-striatal INT maps were correlated ($r= 0.45$). At the voxel level, the INT values closely matched the average INTs of their top 10 strongest cortical connections.

Overall, we demonstrated that INTs are organized along spatial gradients that closely

match FC gradients.

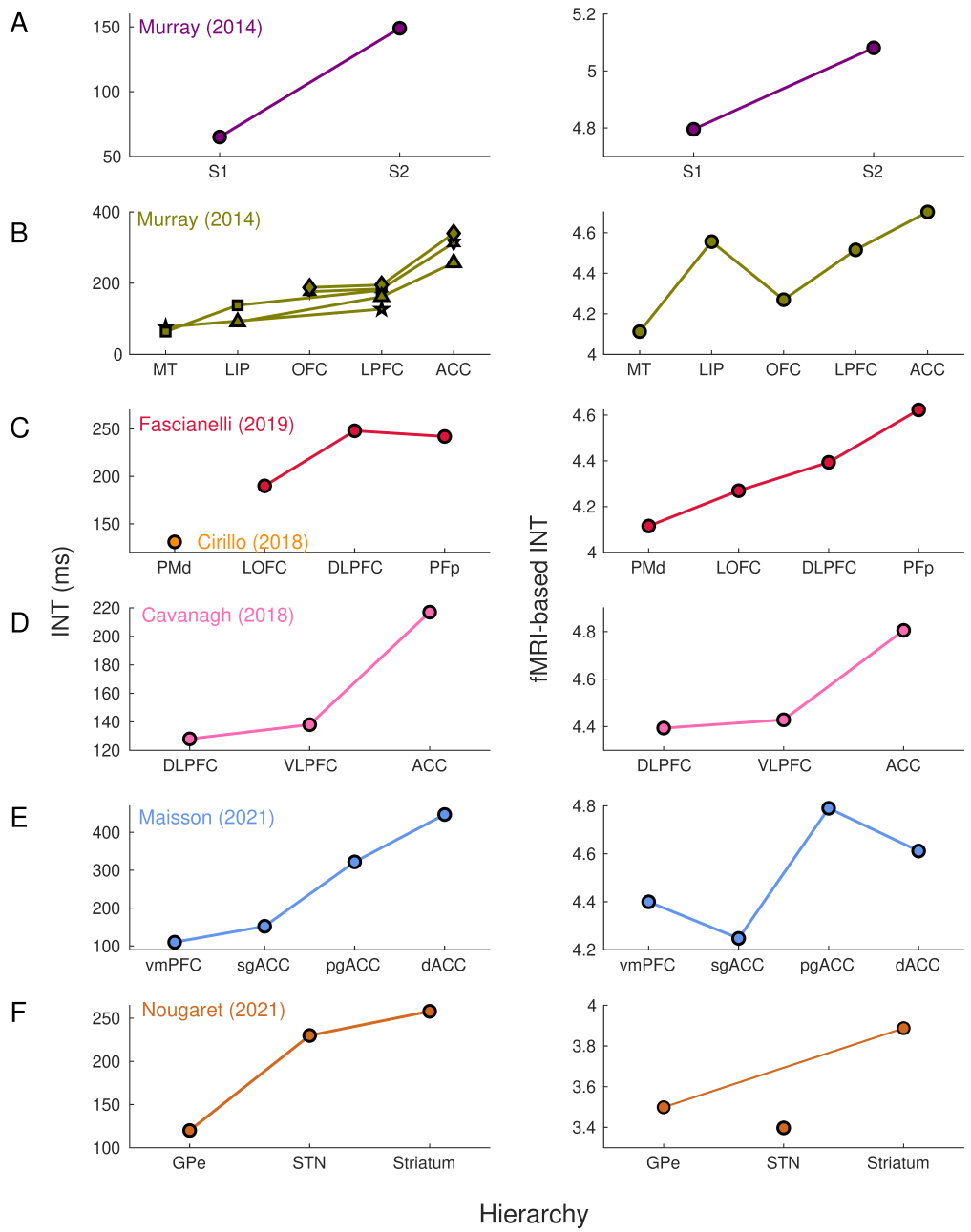

Figure 1. Intrinsic neural timescales estimated from fMRI and electrophysiology reveal a similar hierarchical ordering of cortical and subcortical areas.

Group-averaged (N=9) intrinsic neural timescales (INTs) were estimated for each area of interest by averaging across voxels. Each color represents a hierarchy estimated from a different electrophysiology data set (Left). The hierarchies estimated from spiking data were replicated via fMRI (Right). Somatosensory (A) and visual (B) hierarchies reported by Murray et al. (2014) Note: Each symbol represents a different data set as originally reported by the respective authors. Frontal

hierarchy reported by Fascianelli et al. (2019) and Cirillo et al. (2018) (C). Frontal hierarchy reported by Cavanagh et al. (2018) (D). Medial prefrontal hierarchy reported by Maisson et al. (2021) (E). Subcortical hierarchy reported by Nougaret et al. (2021) (F). The areas were defined bilaterally for each panel to match the recording sites of the data set— the Cortical Hierarchy Atlas of the Rhesus Macaque (Jung et al., 2021) and Subcortical Atlas of the Rhesus Macaque (Hartig et al., 2021) were used when possible (see Supplementary File 1). The hemodynamic INTs were estimated as the sum of the autocorrelation function (ACF) values in the initial positive period- i.e., this measurement considers both the number of lags and the magnitude of the ACF values. Hence, the INT does not have a time unit and it is used as a proxy of the timescale of that area, with higher values reflecting longer timescales. See Figure 1 Supplement 2 for an estimate of the time constant of each area. The INT of individual areas were estimated by taking the average of the voxels' INT values. The analysis was performed at the group level (N = 9). Abbreviations: S1/S2 (primary/secondary somatosensory cortex), MT (middle temporal area), LIP (lateral intraparietal area), OFC (orbitofrontal cortex), LPFC (lateral prefrontal cortex), ACC (anterior cingulate cortex), PMd (dorsal premotor cortex), LOFC (lateral OFC), DLPFC (dorso-lateral PFC), VLPFC (ventro-lateral PFC), PFp (polar prefrontal cortex), vmPFC (ventro-medial PFC), sgACC (subgenual ACC), pgACC (pregenual ACC), dACC (dorsal ACC), GPe (external globus pallidus), STN (subthalamic nucleus). Figure 1 Supplement 3 depicts single-subject INT stability and similarity and the group-level stability of the INT hierarchies.

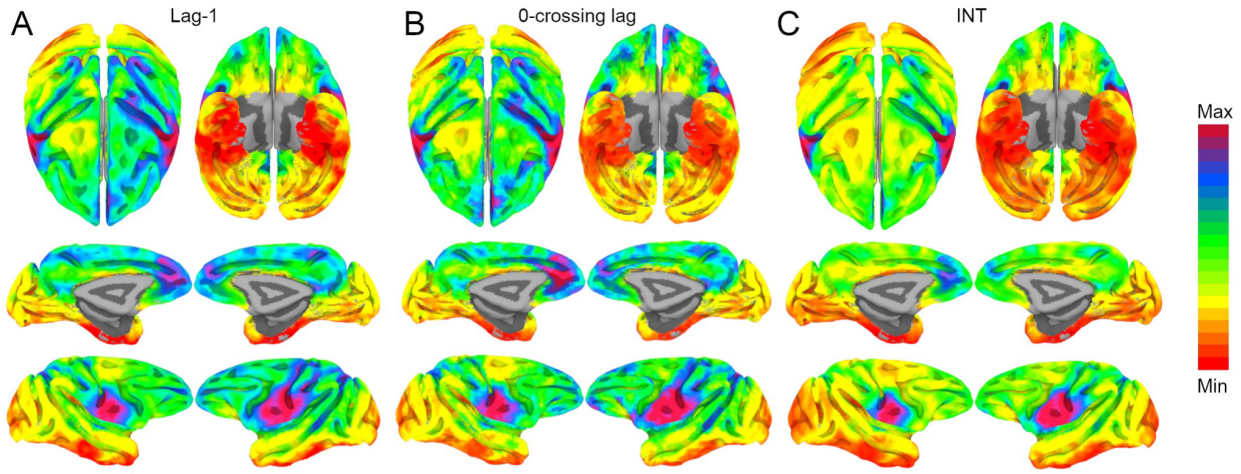

Figure 1 Supplement 1. Whole-brain hemodynamic intrinsic neural timescales, lag-1 and 0-crossing lag.

The hemodynamic intrinsic neural timescales (INTs) were estimated as the sum of the autocorrelation function (ACF) values in the initial positive period. This approach considers both the magnitude (quantified as the lag-1 ACF value) and the timescale (quantified as the 0-crossing lag). To examine whether one of these components is a stronger driver of our INT measurement, the lag-1 ACF value (A; Min: 0.93 - Max: 0.96) and the 0-crossing lag (B; Min: 5 - Max: 12) were compared to the INTs (C; Min: 3.3 - Max: 6). The voxel-wise maps were highly correlated: Pearson's r A-B: 0.96; Pearson's r B-C: 0.97; Pearson's r A-C: 0.96. The maps were computed at the group level (N=9). Overall, the magnitude and timescale components of the INTs are highly related. The color bar indicates the lag-1 ACF values, the 0-crossing lag or INTs (Note: Since the hemodynamic INTs were estimated as the sum of ACF values in the initial positive period, this measurement considers both the number of lags and the magnitude of the ACF values. As a result, the INT does not have a time unit and it is used as a proxy of the timescale of that area, with higher values reflecting longer timescales.

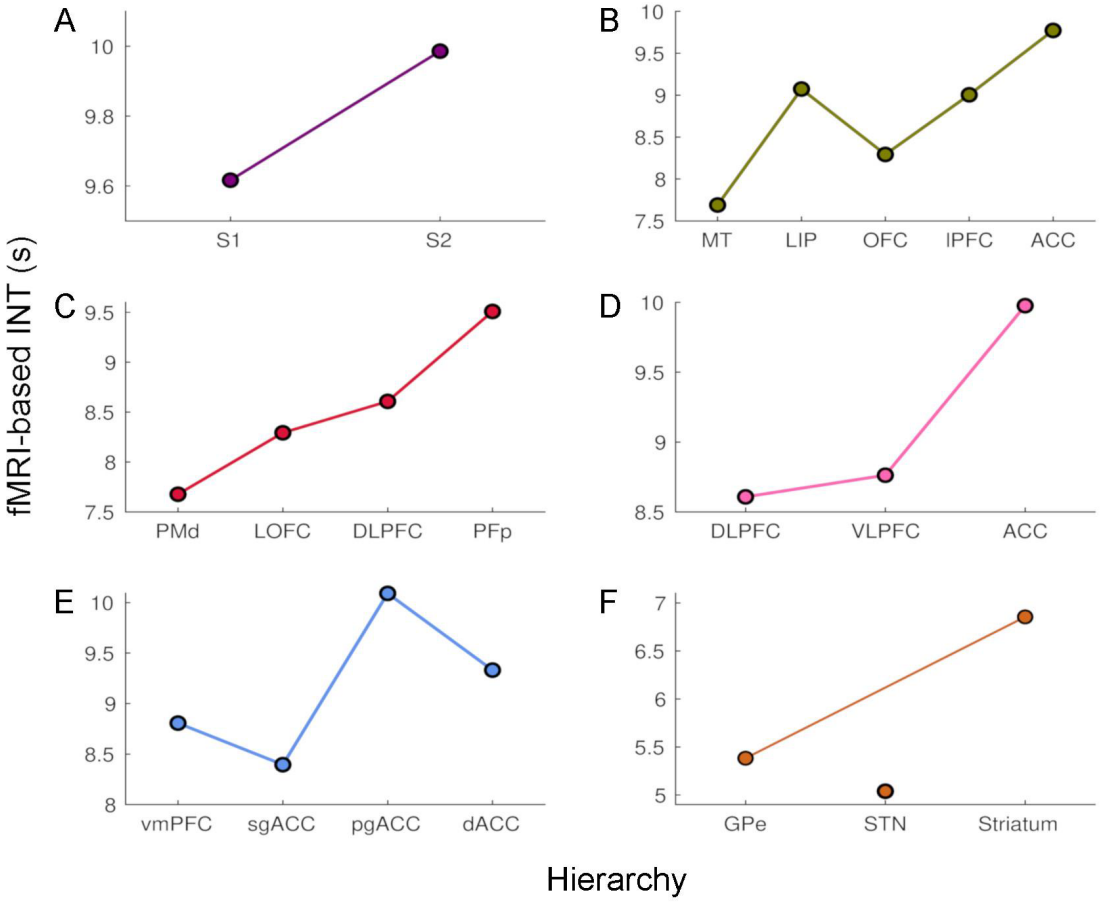

Figure 1 Supplement 2. The time constants of hemodynamic intrinsic neural timescales.

The colors are consistent with the hierarchies from Figure 1. The time constant was operationalized as the 0-crossing lag multiplied by the repetition time (TR = 1.1 s). The relative ordering of the areas is consistent with that based on our intrinsic neural timescale (INT) measure. The analysis was performed at the group level (N = 9). Abbreviations: S1/S2 (primary/secondary somatosensory cortex), MT (middle temporal area), LIP (lateral intraparietal area), OFC (orbitofrontal cortex), LPFC (lateral prefrontal cortex), ACC (anterior cingulate cortex), PMd (dorsal premotor cortex), LOFC (lateral OFC), DLPFC (dorso-lateral PFC), VLPFC (ventro-lateral PFC), PFp (polar prefrontal cortex), vmPFC (ventro-medial PFC), sgACC (subgenual ACC), pgACC (pregenual ACC), dACC (dorsal ACC), GPe (external globus pallidus), STN (subthalamic nucleus).

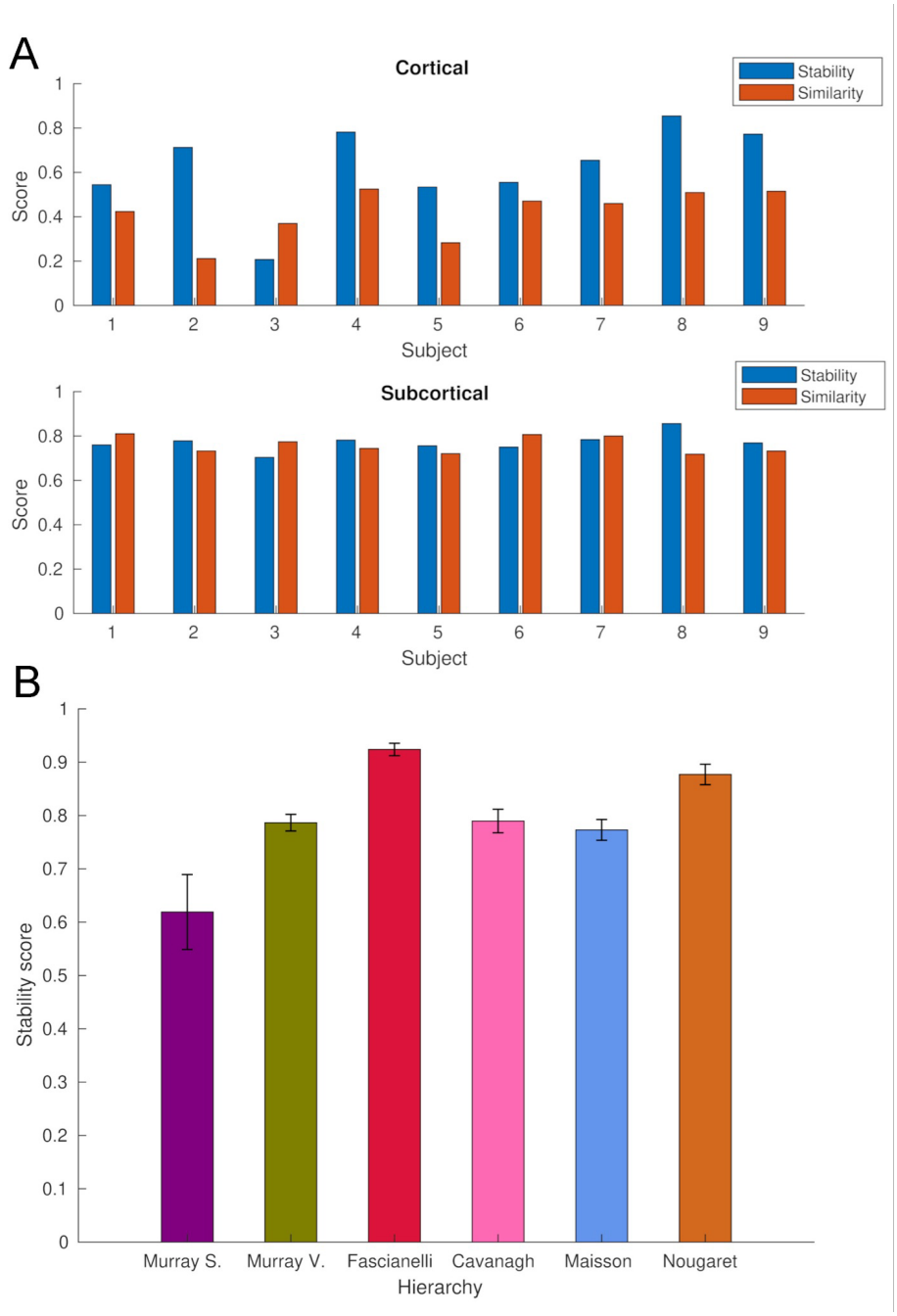

Figure 1 Supplement 3. Stability and similarity analysis of whole-brain intrinsic neural timescales.

(A) Single-subject stability and similarity of cortical (Top) and subcortical (Bottom) intrinsic neural timescales (INTs). The stability score was estimated by averaging Fisher's Z-transformed pairwise Pearson's correlation coefficients across runs. The similarity score was estimated by averaging the Fisher's Z transformed pairwise Pearson's correlation coefficients with all the other subjects. (B) The stability of fMRI-based INT hierarchies (see Figure 1). To estimate stability, the

hierarchies were re-computed for all the possible combinations of groups of four subjects (n = 126) steps). For each step, the Spearman's Rank correlation between the group (N = 9, see Figure 1) and the sub-group (N = 4) hierarchies was computed. The stability score was estimated by averaging the correlation coefficients across steps. Abbreviations: Murray S. (Murray et al., 2014; Somatosensory hierarchy), Murray V. (Murray et al., 2014; Visual hierarchy); Fascianelli (Fascianelli et al. 2019; and Cirillo et al., 2018); Cavanagh (Cavanagh et al., 2018); Maisson (Maisson et al., 2021); Nougaret (Nougaret et al., 2021).

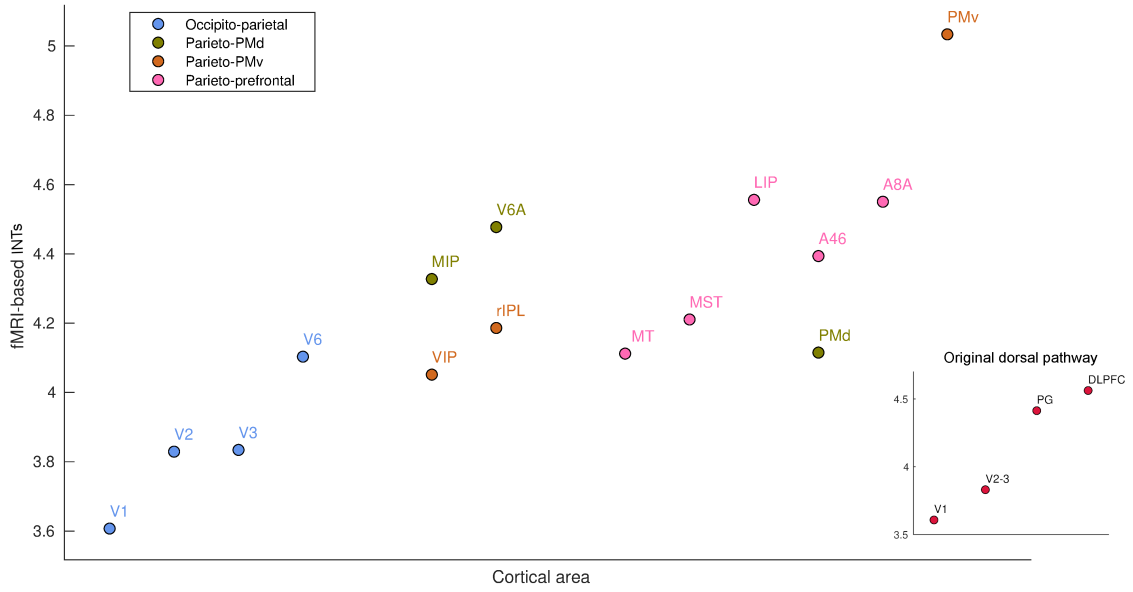

Figure 2. fMRI reveals a hierarchical ordering of timescales in the dorsal pathway for visuospatial processing.

Group-averaged (N=9) intrinsic neural timescales (INTs) were estimated for each area of interest by averaging across voxels. The areas were defined bilaterally based on the Cortical Hierarchy Atlas of the Rhesus Macaque (Jung et al., 2021) (see Supplementary File 2). The dorsal pathway reveals a gradual progression of INTs from sensory to association and motor cortices. The hierarchical pattern of INTs can be observed in the original description of the dorsal pathway (inset), but also in more recently described subdivisions. Every color represents a subdivision of the dorsal pathway as described in Kravitz, Saleem, Baker, & Mishkin (2011). Note: Since the hemodynamic INTs were estimated as the sum of ACF values in the initial positive period, this measurement considers both the number of lags and the magnitude of the ACF values. As a result,

the INT measure does not have a time unit and it is used as a proxy of the timescale of that area, with larger values reflecting longer timescales. Abbreviations: DLPFC (dorso-lateral prefrontal cortex), VIP (ventral intraparietal area), MIP (medial intraparietal area), rIPL (rostral inferior parietal lobule, MT (middle temporal area), MST (medial superior temporal area), LIP (lateral intraparietal area), A46 (area 46), A8A (area 8A), PMd (dorsal premotor cortex), PMv (ventral premotor cortex).

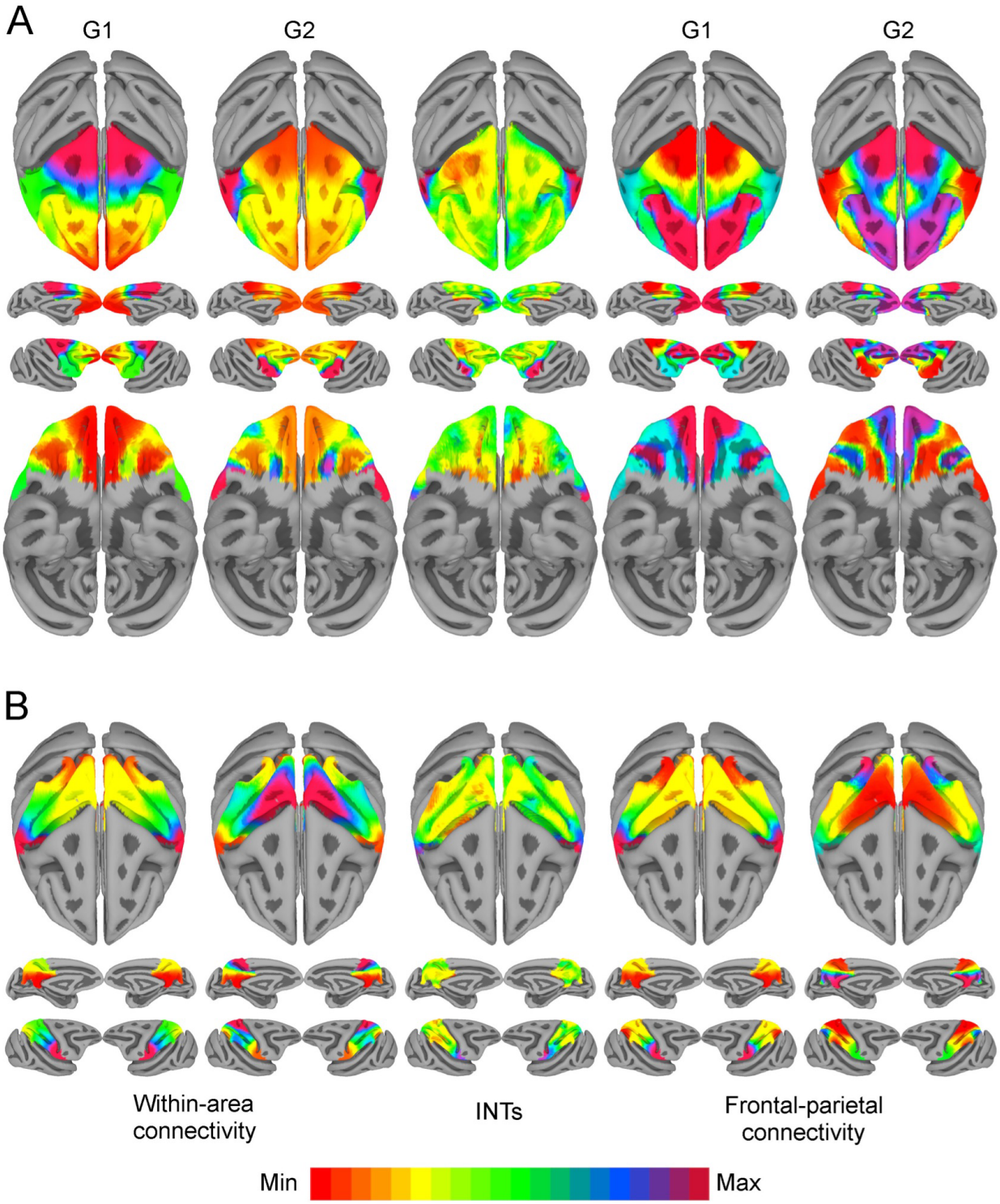

Figure 3. Functional connectivity gradients are related to intrinsic neural timescale topographies. Intrinsic neural timescale (INT) maps (Middle) and functional connectivity (FC) gradients were computed at the group level (N=9). Gradient 1 (G1) and Gradient 2 (G2) were estimated using a

cosine similarity affinity computation of the within-area FC (Left) and frontal-parietal FC (Right), followed by diffusion mapping (Note: G1 and G2 are the first components that describe the axes of largest variance). (A) Frontal INTs were correlated with G2 for both within-area (r= 0.47) and frontal-parietal connectivity (r= -0.26). (B) Parietal INTs were correlated with G1 for both within-area (r= 0.56) and parietal-frontal connectivity (r= 0.47). The color bar indicates the position along the FC gradient (Note: values are on an arbitrary scale) or INT values (Note: since the hemodynamic INTs were estimated as the sum of ACF values in the initial positive period, this measurement considers both the number of lags and the magnitude of the ACF values. As a result, the INT does not have a time unit and it is used as a proxy of the timescale of that area, with larger values reflecting longer timescales). The value ranges differ across panels unless otherwise stated.

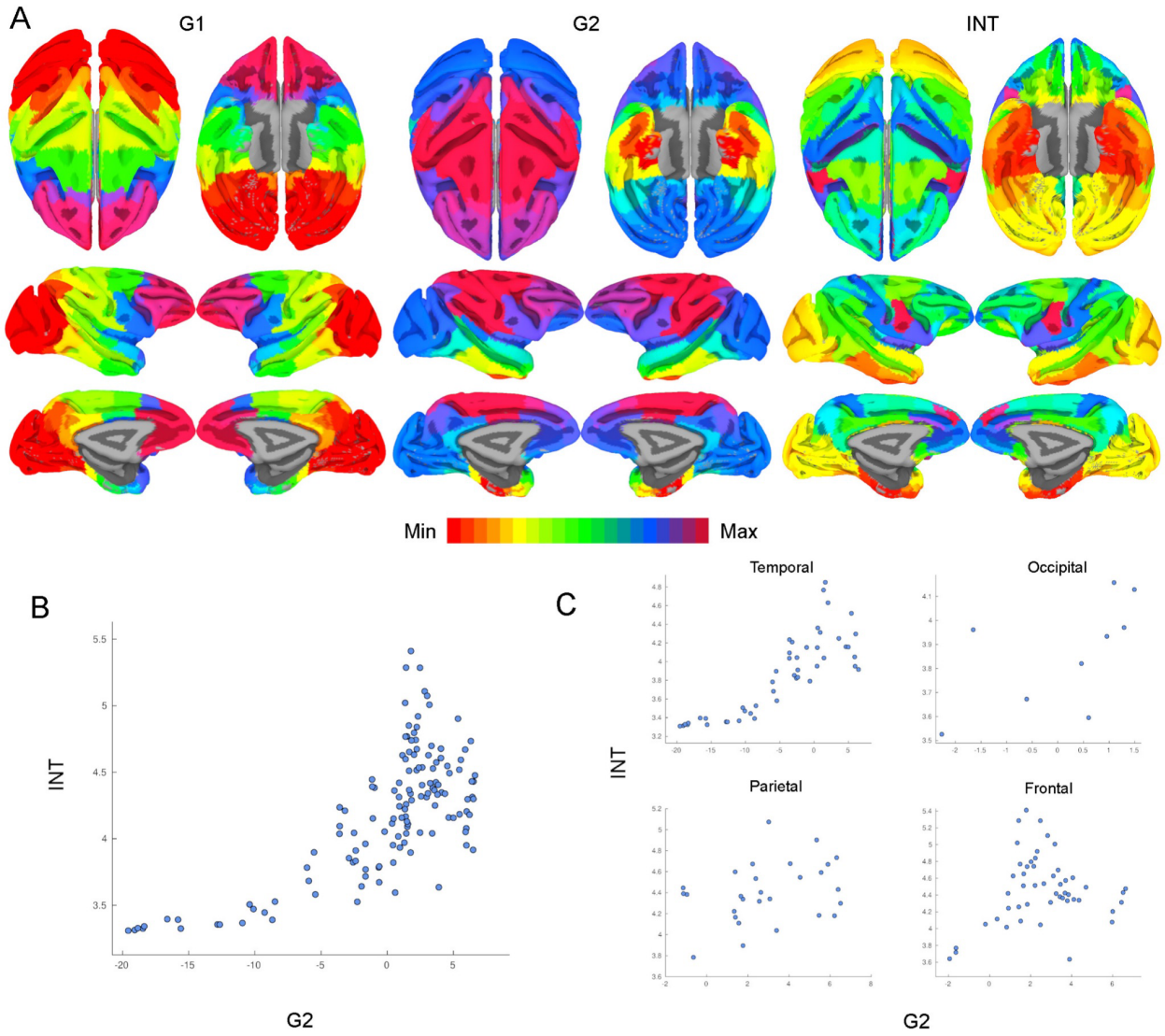

Figure 3 Supplement 1. Intrinsic neural timescales are topographically organized along functional connectivity gradients across the whole cortex.

(A) The first (G1; Left) and second (G2; Middle) functional connectivity (FC) gradients estimated at the whole-cortex level, and the intrinsic neural timescale (INT) map. The brain was parcellated using the Cortical Hierarchy Atlas of the Rhesus Macaque (Level 6; Jung et al., 2021) and the connectivity matrix was constructed by computing the Pearson's correlation of the resulting time series (134x134 connectivity matrix). G1 and G2 were estimated using a cosine similarity affinity computation of this connectivity matrix, followed by diffusion mapping (Note: G1 and G2 are the first components that describe the axes of largest variance). The INT of individual parcels were estimated by taking the average of the voxels' INT values. The analysis was performed at the group level (N = 9). The INT map was highly correlated with G2 (Pearson's r = 0.70), and to a lesser extent to G1 (Pearson's r = 0.20). The color bar indicates the position along the FC gradient (Note: values are on an arbitrary scale) or INT values (Note: since the hemodynamic INTs were estimated as the sum of ACF values in the initial positive period, this measurement considers both the number of lags and the magnitude of the ACF values. As a result, the INT does not have a time unit and it is used as a proxy of the timescale of that area, with larger values reflecting longer timescales). The value ranges differ across panels. (B) At the parcel level, there is a monotonic relationship between INT and G2 values. (C) The INT and G2 values are monotonically related within each lobe. Note: the subplots are a decomposition of the scatter plot in (B) into the four lobes.

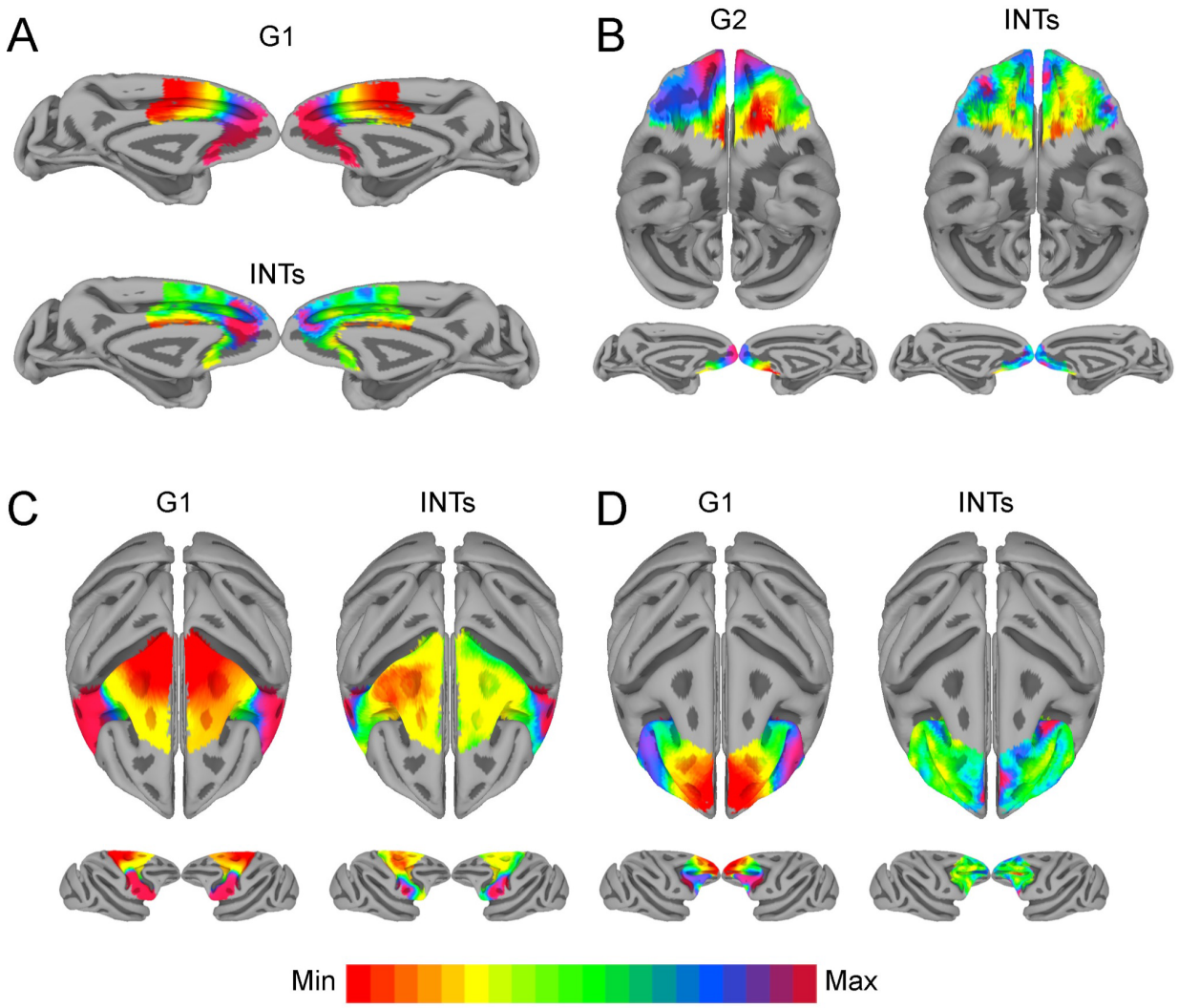

Figure 4. The relationship between functional connectivity and intrinsic neural timescales in the frontal lobe.

Group-averaged intrinsic neural timescale (INT) maps (Right) and functional connectivity (FC) gradients (Left) were estimated at the group level (N=9). Gradient 1 (G1) and Gradient 2 (G2) were estimated using a cosine similarity affinity computation of the within-area followed by diffusion mapping (Note: G1 and G2 are the first components that describe the axes of largest variance). The FC gradient with the highest correlation to INTs was plotted. (A) INTs in medial prefrontal cortex were correlated with G1 (r= 0.49). (B) INTs in the orbitofrontal cortex were correlated with G2 (r= 0.45). (C) INTs in the motor cortex were correlated with G1 (r= 0.68) (D) INTs in the lateral prefrontal cortex were correlated with G1 (r = 0.35). The color bar indicates the position along the FC gradient (values are on an arbitrary scale) or INT values (Note: since the

hemodynamic INTs were estimated as the sum of ACF values in the initial positive period, this measurement considers both the number of lags and the magnitude of the ACF values. As a result, the INT does not have a time unit and it is used as a proxy of the timescale of that area, with larger values reflecting longer timescales). The value ranges differ across panels unless otherwise stated. For a more in-depth analysis of the relationship between INTs and FC see Figure 4 Supplement 1. For the single-subject analysis see Figure 4 Supplement 2.

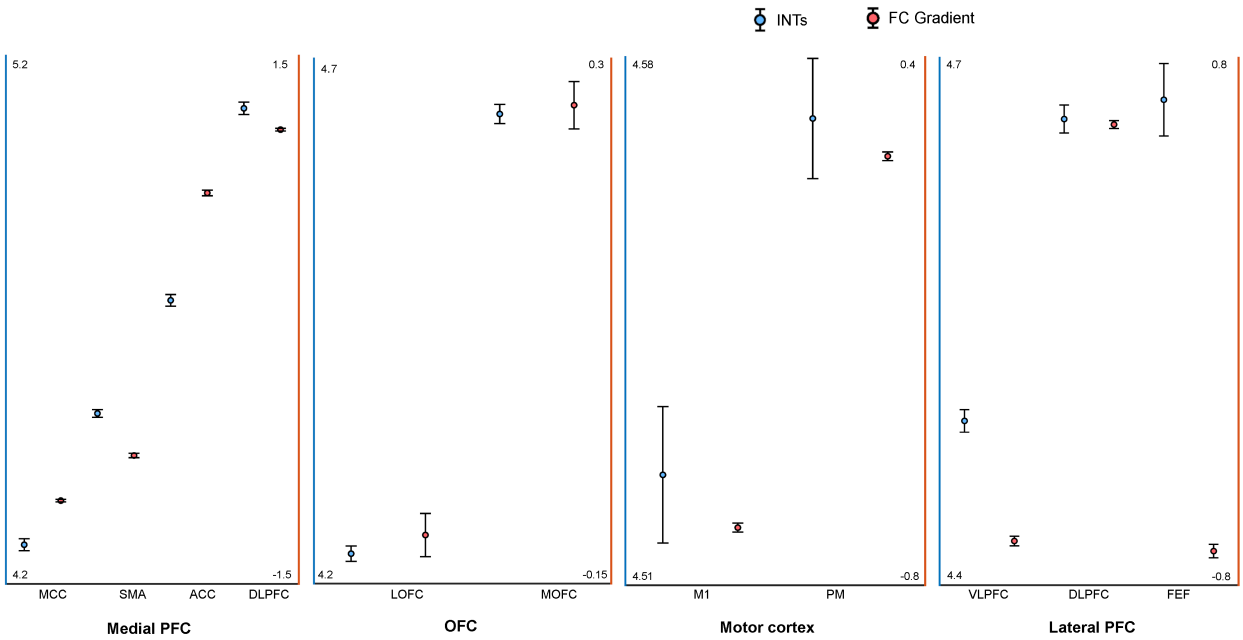

Figure 4 Supplement 1. Intrinsic neural timescales and functional connectivity gradients are monotonically related in the frontal lobe.

For a better interpretation of the relationship between the intrinsic neural timescale (INT) maps and (functional connectivity) FC gradients, the INT/gradient values were averaged across voxels within the functional subdivisions of the areas considered in Figure 4. The functional subdivisions were defined based on the Cortical Hierarchy Atlas of the Rhesus Macaque (CHARM; Jung et al., 2021). The error bars represent ±1 Standard Error (SE; calculated as the standard deviation divided by the square root of the number of voxels). The blue circles represent INT values (left Y-axis) and the red circles represent the FC gradient value (right Y-axis). In the medial wall of the PFC, both INT and gradient values roughly change in an anterior-posterior direction with the slowest timescales found in the anterior and the fastest timescales in the posterior regions (Note: both SMA and pre-SMA were included). In the OFC, both INT and gradient values have a medio-lateral axis

of change, with the slowest timescales in the MOFC and fastest timescales in the LOFC. In the lateral motor cortex, both the INT and gradient values increase in a medio-lateral way, with M1 having the fastest and PM the slowest timescales. In the lateral prefrontal cortex, the INT values are decreasing from FEF to the VLPFC while the gradient values are decreasing from FEF/VLPFC to the DLPFC. The plots are based on the INT and gradient maps derived at the group level (N = 9) (Note: the plots were derived from the maps in Figure 4). Abbreviations and CHARM codes**:** FEF (frontal eye fields; Level 3 Code 51), DLPFC (dorsolateral prefrontal cortex; Level 3 Code 54), VLPFC (ventrolateral prefrontal cortex; Level 3 Code 64), M1 (primary motor cortex; Level 4 Code 79), PM (premotor cortex; level 4 Code 80), MOFC (medial orbitofrontal cortex; Level 3 Code 17), LOFC (lateral orbitofrontal cortex; Level 3 Code 25), ACC (anterior cingulate cortex; Level 3 Code 3), SMA (supplementary motor area; Level 3 Code 87), MCC (midcingulate cortex; Level 3 Code 11).

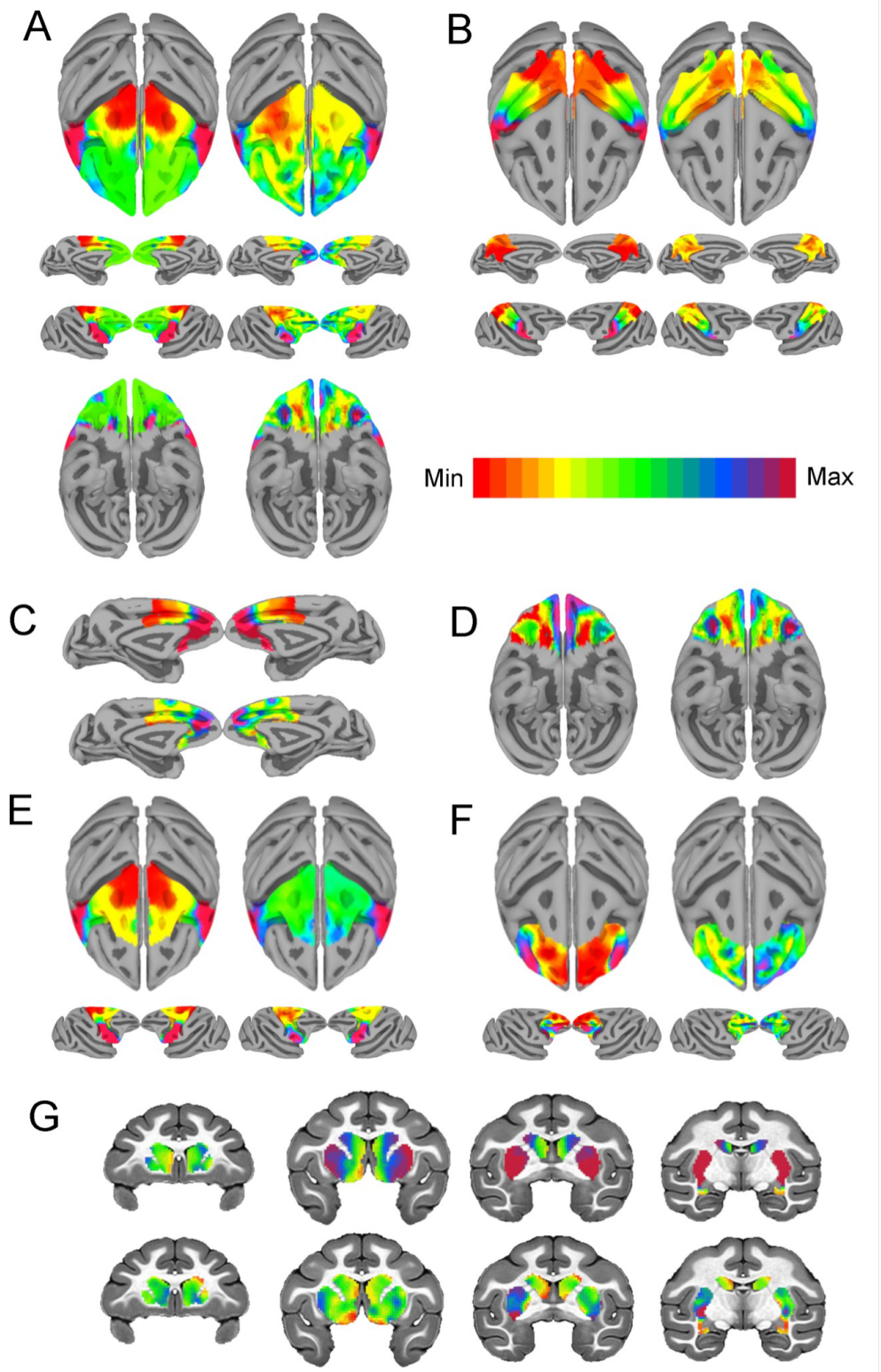

Figure 4 Supplement 2. Intrinsic neural timescales closely match functional connectivity gradients at the single-subject level.

The within-area (Right, A-F) and cortico-striatal (Top, G) functional connectivity (FC) gradient, and corresponding intrinsic neural timescale (INT) map (Left) (Note: the gradient with the highest correlation to INTs is depicted). Similar to the group results, INTs were related to FC gradients across the whole brain: frontal lobe (A, r = 0.66); parietal lobe (B, r = 0.81); medial PFC (C, r = 0.62); orbitofrontal cortex (D, r = 0.51); motor cortex (E, r = 0.89); lateral PFC (F, r = 0.29); striatum (G, r = 0.47). The color bar indicates the position along the FC gradient (Note: values are on an arbitrary scale) or INT values (Note: since the hemodynamic INTs were estimated as the sum of ACF values in the initial positive period, this measurement considers both the number of lags and the magnitude of the ACF values. As a result, the INT does not have a time unit and it is used as a proxy of the timescale of that area, with larger values reflecting longer timescales). The value ranges differ across panels unless otherwise stated.

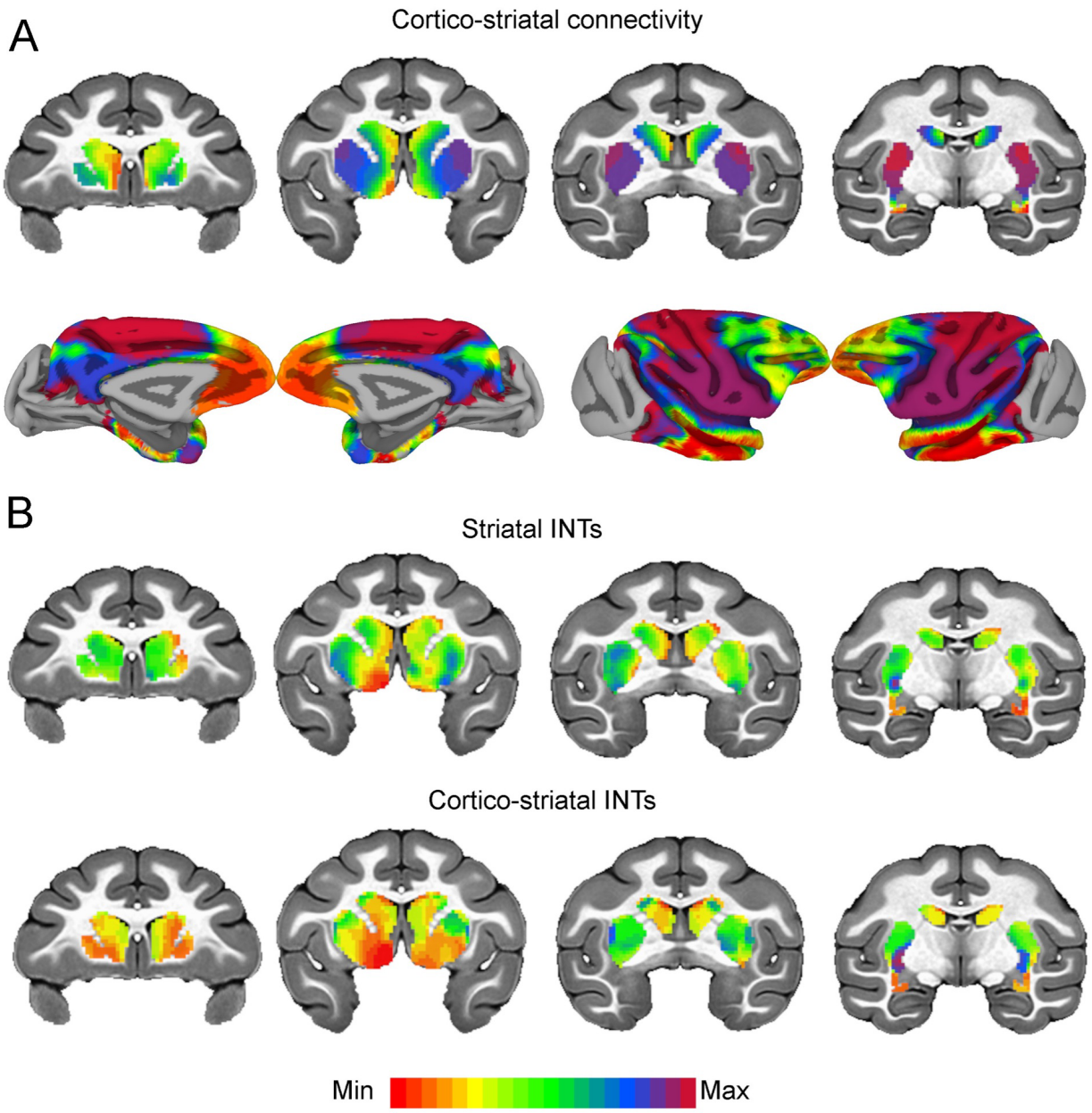

Figure 5. Cortico-striatal functional connectivity is related to intrinsic neural timescales. Group-averaged intrinsic neural timescale (INT) maps and functional connectivity (FC) gradients (Left) were estimated at the group level (N=9). Gradient 1 (G1) and Gradient 2 (G2) were estimated using a cosine similarity affinity computation of the cortico-striatal FC followed by diffusion mapping (Note: G1 and G2 are the first components that describe the axes of largest variance). Only the gradient with the highest correlation to the striatal INT map was plotted. (A) The striatal FC gradient estimated from cortico-striatal connectivity (Top) and its projection onto

the cortex (Bottom) (Note: the same value range was used). The FC patterns underlying the cortico-striatal gradient matched the anatomical connectivity derived from animal invasive tracing. (B) Striatal INTs (Top) and cortical INTs projection based on cortico-striatal FC (Bottom). The striatal and cortico-striatal INT maps were related (r= 0.45). Striatal INTs were related to G1 estimated from cortico-striatal connectivity (r= 0.38). The color bar indicates the position along the FC gradient (values are on an arbitrary scale) or INT values (Note: since the hemodynamic INTs were estimated as the sum of ACF values in the initial positive period, this measurement considers both the number of lags and the magnitude of the ACF values. As a result, the INT does not have a time unit and it is used as a proxy of the timescale of that area, with larger values reflecting longer timescales). The value range differs across panels unless otherwise stated.

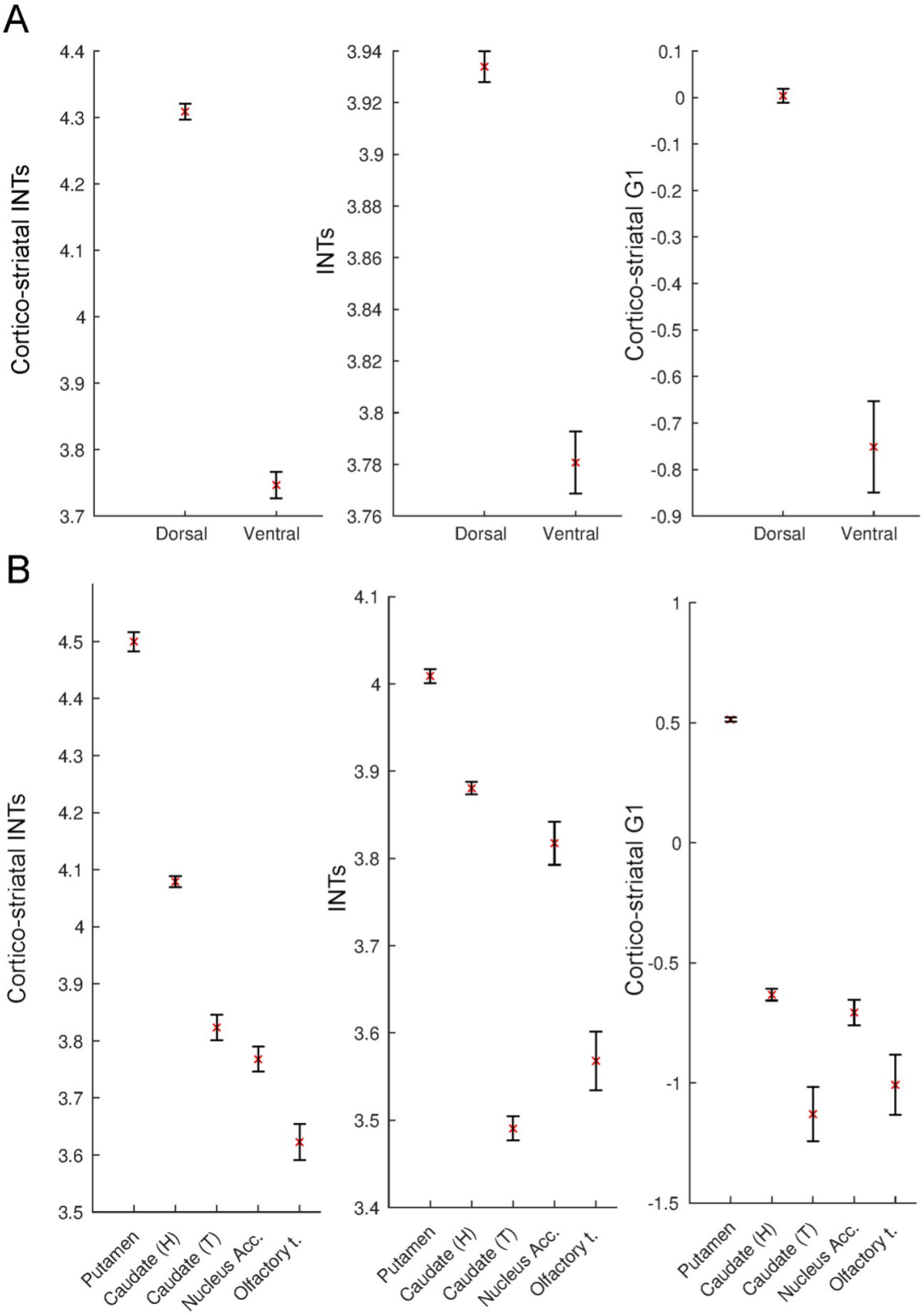
A
Cortico-striatal INTs
INTs
Cortico-striatal G1
Dorsal
Ventral
B
Putamen
Caudate (H)
Caudate (T)
Nucleus Acc.
Olfactory t.

Figure 5 Supplement 1. Intrinsic neural timescales and functional connectivity gradients are monotonically related in the striatum.

For a better interpretation of the relationship between the striatal and cortico-striatal intrinsic neural timescale (INT) maps and functional connectivity (FC) gradients, the INT/gradient values were averaged across voxels within the functional subdivisions of the striatum. The functional subdivisions were defined based on the Subcortical Atlas of the Rhesus Macaque (SARM; Hartig et al., 2021). The error bars represent 2*Standard Error (SE; calculated as the standard deviation divided by the square root of the number of voxels). (A) Dividing the striatum into its major functional subdivisions revealed that for both striatal and cortico-striatal INTs and FC, there is a dorsal to ventral axis of change. The dorsal striatum had the slowest and ventral striatum the fastest timescales, which was reflected in both the striatal and cortico-striatal INTs. (B) A finer subdivision of the striatum reveals a similar ventro-dorsal but also medio-lateral axis of change across the three maps. While the striatal INTs and the FC gradient have a very good correspondence, the head of the caudate in the cortico-striatal INT map deviates from this pattern - i.e., it has higher values relative to the other structures in the ventral striatum. The plots are based on the INT and gradient maps derived at the group level (N = 9). Note: since the hemodynamic INTs were estimated as the sum of ACF values in the initial positive period, this measurement considers both the number of lags and the magnitude of the ACF values. As a result, the INT does not have a time unit and it is used as a proxy of the timescale of that area, with larger values reflecting longer timescales. Abbreviations and SARM codes: Caudate (H) (head of the caudate; Level 6 Code 46); Caudate (T) (tail of the caudate; Level 6 Code 47); Nucleus Acc. (nucleus accumbens; Level 6 Code 52); Olfactory T. (olfactory tubercule; Level 6 Code 53), Dorsal Striatum (Level 4 Code 44), Ventral Striatum (Level 4 Code 51), G1 (Gradient 1).

3. Discussion

Temporal integration is a fundamental property of neural processing (Cavanagh, Hunt & Kennerley, 2020; Hasson et al., 2008; Honey et al., 2012; Soltani et al., 2021), both during task performance and in the absence of external stimulation (Cirillo et al., 2018; Hasson et al., 2008; Murray et al., 2014; Raut et al., 2020; Ito, Hearne, & Cole, 2020). However, until this point, there have been major gaps in investigating temporal integration across the brain, across species, and across populations. This is because, traditionally, temporal integration has been studied primarily using single-unit electrophysiology in NHPs (although see Gao, van den Brink, Pfeffer, & Voytek, 2020). Although there is some evidence that BOLD signals from fMRI may allow for whole brain interrogation of timescales in humans (Watanabe et al., 2019; Wengler et al., 2020), such an approach had not yet been validated. Here, we focused on investigating whole-brain INT and FC topographies at different levels of description, to first validate, within-species, the study of INTs using BOLD fMRI, and then investigate the relationship between temporal and spatial dynamics of the resting brain with ultrahigh resolution fMRI across the whole macaque brain.

We have demonstrated the feasibility of estimating INTs from fMRI in the NHP brain. We did so by showing that hemodynamic INT hierarchies closely match those derived from NHP electrophysiology. While some recent human neuroimaging studies have investigated whole-brain hemodynamic INTs (Raut et al., 2020; Watanabe et al., 2019; Wengler et al., 2020), temporal hierarchies derived from electrophysiology have not been replicated via fMRI, nor within species. Furthermore, in a previous paper, INTs derived from fMRI data in human subjects were elegantly validated with EEG (Watanabe et al., 2019). The present findings are in agreement with these results, finding slower and shorter INTs in frontoparietal areas and sensory-related areas, respectively. This points towards cross-species homologies in cortical INTs, hence laying the groundwork for future translational work. Nevertheless, the step presented here is essential, because we were able to demonstrate the equivalence of the fMRI estimates of INT hierarchies with single neuron spiking results within the same species. This finding provides validation for the complementary use of hemodynamic and electrophysiological INTs. Using fMRI in this context has several advantages. First, it can be performed on the whole brain. Second, it can easily be employed across different human populations in the future, dramatically expanding the possible uses of INT investigations.

We did observe minor deviations from electrophysiological INTs in our data. These may be in large part attributable to a high degree of INT heterogeneity within individual anatomical regions. This observation is in line with previous reports of heterogeneity within neural populations in single-unit recordings (Cirillo et al., 2018; Nougaret et al., 2021). This suggests that averaging INTs within anatomical regions might not provide a full description of macroscale organization.

It is worth noting that the current study could not resolve the exact correspondence between the time constants estimated from spiking activity and BOLD. The relationship between neural activity and the BOLD signal has been revealed via simultaneous electrophysiological-fMRI recording—i.e., a spatially localized increase in the fMRI signal directly and monotonically reflects an increase in neural activity, with the mean onset time of the BOLD signal relative to the neural activation being 2s (Logothetis, Pauls, Augath, Trinath, & Oeltermann, 2001). As a result of sensory stimulation, BOLD signal is delayed by ~ 2-3 s, followed by a ramp of 6-12 s to a plateau or peak value. Local field potentials (LFPs), and to a lesser extent multi-unit activity, can predict the BOLD signal when convolved with the neuro-vascular impulse response function. In sum, the hemodynamic response is roughly a low-pass-filtered expression of the total neural activity; with LFPs however, having a greater contribution to the signal. This has several implications for the interpretation of hemodynamic timescales: (1) they are more likely to reflect timescales related to LFPs rather than spiking activity; (2) the time constants estimated from spiking activity might not be linearly related to those estimated from fMRI. A further complication for the interpretability of hemodynamic timescales is that INTs have only been estimated from spiking activity, but not LFPs. The exact relationship between timescales derived from spiking activity, LFPs and the BOLD signal remains an empirical question. We hypothesize that hemodynamic timescales generally increase monotonically with those estimated from electrophysiology. In that respect, Watanabe & Masuda (2019) bring preliminary evidence—i.e., timescales derived from electroencephalography (EEG) and fMRI have been shown to differ by two orders of magnitude. This is reasonable considering the BOLD time course-when convolved with the hemodynamic response function, the INTs estimated from EEG were similar in magnitude to those estimated from fMRI. Nevertheless, we show that temporal hierarchies are a general principle of organization, irrespective of the method used to estimate them.

To further demonstrate the potential of INTs estimated from fMRI, we extend the current literature by providing a finer description of the hierarchy of visual INTs compared to those previously described with electrophysiology (Murray et al., 2014). Remarkably, areas along the dorsal visual pathway follow the INT hierarchical ordering predicted by functional specialization and connectivity (Kravitz et al., 2011), with primary visual areas showing the fastest timescales and prefrontal areas showing the longest. Our findings bring further evidence that the dorsal pathway is not a unitary system, but rather subdivided into multiple parallel pathways (Binkofski & Buxbaum, 2013; Kravitz et al., 2011). This demonstrates the importance of fine-grained, large-scale descriptions of the brain for uncovering multiple hierarchies.

We investigated timescales and connectivity topographies at different levels of description to probe whether one aspect of the multi-dimensional functional architecture of the brain is related to temporal structure. We show that INT topographies are closely related to the overlapping FC gradient dimensions. Previous studies have demonstrated that FC gradient dimensions in sensory cortex corresponded with known organizational principles such as eccentricity and polar angle (Haak et al., 2018). Moreover, FC gradients followed M1's somatotopic map. Our findings put forward a significantly more unified framework that generalizes over the entire brain. INTs form a topographic organizational principle ranging from sensory to associative cortex. While other organizational principles can and likely always will be represented across topographic networks of the brain, intrinsic timescales appear to be special in their general extent.

It is noteworthy that there are crucial methodological differences between the gradient and INT estimation approaches: (1) the gradient estimation pipeline consists of multiple steps to reduce the dimensionality of the data, and consequently, the amount of noise (e.g., the FC matrix was made sparse; applying the cosine similarity kernel to build an affinity matrix; and applying a non-linear dimensionality reduction technique to estimate the gradients); (2) the gradients were estimated bilaterally. In comparison to gradients, where the spatial correlation between the voxels' time series is just the initial step in the pipeline, the INT measure consists of the temporal autocorrelation of individual voxels. No extra steps have been taken for noise reduction. Hence, while gradients are the result of a complex processing pipeline, INTs are a relatively simple calculation. As a result, there is a higher amount of variability in the INT maps which could potentially lead to the underestimation of the FC-INT relationship. With respect to the second point, the symmetry of the gradients could be a byproduct of estimating the gradients bilaterally.

Other studies (e.g., Haak et al., 2018; Przeździk et al., 2019) have derived gradients for each hemisphere individually and no major asymmetries have been reported. We estimated the gradients bilaterally because of an issue that is inherent with experimental ultrahigh fields. Specifically, RF transmit field (or B1) inhomogeneities lead to asymmetric signal intensities. We were worried that these effects might introduce asymmetries between the two hemispheres. We have reason to believe that this issue is partially being taken care of by estimating the gradients bilaterally, but the INTs are still susceptible to these effects. This could also result in the underestimation of the FC-INT relationship since there are visible asymmetries in the INT maps.

One potential limitation of the current study is using anesthetized subjects. Although obtaining high resolution images of awake NHPs at ultrahigh fields would be ideal, it is still an enormous technical challenge that the field is working to overcome. Using our low anesthesia strategy, we were able to obtain a relatively large sample size of NHPs (because extensive training was not required). It is important to note that it was previously shown that our anesthesia protocol demonstrates no observable biases to whole-brain connectivity analysis (Yacoub et al., 2020). Moreover, it has been shown that this protocol has a relatively low impact on reproducibility (Autio et al., 2021). To our knowledge, the largest effect of vasodilative anesthetics (such as isoflurane) is an overall blunting of responses which is counteracted by ultrahigh-field MRI. Finally, besides the possible effects on the hemodynamic response, anesthesia introduces a crucial difference between the current study and previous research – while in previous studies it was not controlled for the subjects engaging in various cognitive processes, in anesthetized subjects, this confound is potentially removed. Overall, future research should replicate current results to exclude a possible effect of anesthesia.

We show that resting-state fMRI in NHPs is crucial for bridging the gap between human and animal models, but also across the various techniques of investigating the brain. Nevertheless, macaques have a disadvantage as a model organism for fMRI because of their small head size (~6% of the human brain) which makes the use of standard field strength magnets problematic for acquiring high-resolution data. As a result, collecting high-resolution, high SNR whole-brain data has been extremely difficult (Yacoub et al., 2020). We show here that one way of overcoming this problem is to use ultrahigh field strengths in combination with high channel count receiver arrays (Lagore et al., 2021; Uğurbil et al., 2019; Yacoub et al., 2020). Ultrahigh magnetic fields not only enhance SNR but also increase the BOLD contrast, especially for the microvascular BOLD

contributions-which leads to mapping signals with higher precision to sites of neuronal activity (Ugurbil, 2016; Uğurbil, 2018). In conclusion, our unique approach made it possible to obtain whole-brain high-resolution data to investigate FC and INTs across both cortical and subcortical structures.

INTs, like anatomical connectivity and FC, are one way of characterizing the organization of the brain. Critically, combined maps of all three will require a nonhuman animal model such as the macaque, as anatomical connectivity cannot be directly measured in humans (Grier, Zimmermann & Heilbronner, 2020). It is clear that anatomical connectivity, FC, and INTs are related, although the precise nature of the relationships is somewhat speculative. For instance, vertex FC strength is related to human INTs estimated from fMRI (Raut et al., 2020). Our own results show that cortico-striatal INTs and FC gradients broadly track anatomical connectivity. Anatomical connectivity establishes the pathways which the signals underpinning FC use. However, the fact that the pathways exist and are used does not tell us what types of information transformations occur along the way. Through cascaded processing, longer and longer TRWs can be built, measured as longer INTs. Thus, we expect that the space of potential INTs is constrained by both anatomical and functional connectivity. Future exploration of these organizational principles, including using pharmacological interventions and electrical stimulation, will likely clarify the causal relationships at play.

We show that INTs are topographically organized along FC gradients throughout the NHP brain. Although we focused our analysis on the frontal and parietal lobes, and the striatum, we also showed that a whole-brain analysis recapitulates the same conclusion: resting-state temporal and spatial dynamics are closely related. Future investigations should examine this relationship in other cortical and subcortical brain areas. A promising avenue would be to examine the FC-INT link throughout the brain across different levels of parcellation (and different types of parcellations) While we show that intrinsic timescales are related to FC, other studies have related them to other anatomical and functional markers (e.g., see Ito. et al., 2020; Watanabe et al., 2019). Hence, further investigations and careful experimentation are needed to understand (1) how temporal dynamics relate to other functional and anatomical characteristics across the brain; (2) their functional relevance and translational potential.

4. Materials and methods

4.1. Animal preparation

We obtained data from 9 adult macaque monkeys (*Macaca fascicularis*: 5 female, and *Macaca mulatta*, 3 male and 1 female). Weights ranged from 3.0 kg to 9.4 kg. Experimental procedures were carried out in accordance with the University of Minnesota Institutional Animal Care and Use Committee and the National Institute of Health standards for the care and use of NHPs. All subjects were fed *ad libitum* and pair-housed within a light and temperature controlled colony room. Animals were not water restricted. None of the subjects had any prior implant or cranial surgery. Animals were fasted for 14-16 hours prior to imaging.

On scanning days, anesthesia was first induced by intramuscular injection of atropine (0.5 mg/kg), ketamine hydrochloride (7.5 mg/kg) and dexmedetomidine (13 ug/kg). Subjects were transported to the scanner anteroom and intubated using an endotracheal tube. Initial anesthesia was maintained using 1.0-2% isoflurane mixed with oxygen (1L/m during intubation and 2L/m during scanning to compensate for the 12m length of the tubing used). For functional imaging, the isoflurane level was lowered to 1%.

Subjects were placed onto a custom-built coil bed with integrated head fixation by placing stereotactic ear bars into the ear canals. The position of the animal corresponds to the sphinx position. Experiments were performed with animals freely breathing. An initial bolus injection of 1.5ug/kg fentanyl was administered IV followed by a continuous administration of 3ug/kg/hr using a syringe pump. Rectal temperature (~99.6F), respiration (10-15 breaths/min), end-tidal CO2 (25-40), electrocardiogram (70-150 bpm) and SpO2 (>90%) were monitored using an MRI compatible monitor (IRADIMED 3880 MRI Monitor, USA). Temperature was maintained using a circulating water bath as well as chemical heating pads and padding for thermal insulation.

4.2. Data acquisition

All data were acquired on a passively shielded 10.5 Tesla, 88 cm diameter clear bore magnet coupled to Siemens gradients ("SC72" body gradients operating at a slew rate of 200 mT/m/s, and 70 mT/m maximal strength) and electronics (Magnetom 10.5T Plus) (Siemens, Erlangen, Germany). Within the gradient set and the bore-liner, the space available for subject insertion had a 60 cm diameter.

The 10.5T system operates on the E-line (E12U) platform which is directly comparable to clinical platforms (3T Prisma/Skyra, 7T Terra). As such, the user interface and pulse sequences

were identical to those running on clinical platforms. A custom in-house built and designed RF coil with an 8-channel transmit/receive end-loaded dipole array of 18 cm length (individually) combined with a close-fitting 16-channel loop receive array head cap, and an 8-channel loop receive array of 50 × 100mm size located under the chin (Lagore et al., 2021). The size of 14 individual receive loops of the head cap was 37 mm with 2 larger ear loops of 80 mm - all receiver loops were arranged in an overlapping configuration for nearest neighbor decoupling. The resulting combined 32 receive channels were used for all experiments and supported 3-fold acceleration in phase encoding direction. The coil holder was designed to be a semi-stereotaxic instrument holding the head of the animal in a centered sphinx position via customized ear bars. The receive elements were modelled to adhere as close to the surface of the animal's skulls as possible. Transmit phases for the individual transmit channels were fine-tuned for excitation uniformity for one representative mid-sized animal and the calculated phases were then used for all subsequent acquisitions. Magnetic field homogenization (B0 shimming) was performed using a customized field of view with the Siemens internal 3D mapping routines. Multiple iterations of the shims (using the adjusted FOV shim parameters) were performed, and further fine adjustment was performed manually on each animal. Third order shim elements were ignored for these procedures.

In all animals a B1+ (transmit B1) fieldmap was acquired using a vendor provided flip angle mapping sequence (example result in Sup. Fig. 9) and then power calibrated for each individual. Following B1+ transmit calibration, 3-5 averages (23 minutes) of a T1 weighted magnetization prepared rapid acquisition gradient echo protocol (3D MP-RAGE) were acquired for anatomical processing (TR = 3300 ms, TE = 3.56 ms, TI = 1140 ms, flip angle = 5°, slices = 256, matrix = 320 × 260, acquisition voxel size = 0.5 × 0.5 × 0.5 mm^3). Images were acquired using in plane acceleration GRAPPA = 2. A resolution and FOV matched T2 weighted 3D turbo spin echo sequence (variable flip angle) was run to facilitate B1 inhomogeneity correction.

Before the start of the functional data acquisition, five images were acquired in both phase encoding directions (R/L, L/R) for offline EPI distortion correction. Five - six runs of fMRI time series, each consisting of 700 continuous 2D multiband (MB)/Simultaneous Multi SLice (SMS) EPI (Moeller et al., 2010; Setsompop et al., 2012; Uğurbil et al., 2013) functional volumes (TR = 1110 ms; TE = 17.6 ms; flip angle = 60°, slices = 58, matrix = 108 × 154; FOV = 81 × 115.5 mm2; acquisition voxel size = 0.75 × 0.75 × 0.75 mm3) were acquired. Images were acquired with a left-

right phase encoding direction using in plane acceleration factor GRAPPA = 3, partial Fourier = 7/8th, and MB or simultaneous multislice factor = 2 (i.e., the number of simultaneously excited slices = 2). Since macaques were scanned in sphinx positions, the orientations noted here are what is consistent with a (head first supine) typical human brain study (in terms of gradients) but translate differently to the actual macaque orientation.

4.3. Image preprocessing

Image processing was performed using a custom pipeline relying on FSL (Jenkinson, Beckmann, Behrens, Woolrich, & Smith, 2012), ANTs (Avants et al., 2014; Avants, Tustison, Wu, Cook, & Gee, 2011), AFNI (Cox, 1996) and a heavily modified CONN (Whitfield-Gabrieli and Nieto-Castanon, 2012) toolbox. Images were first motion corrected using *mcflirt* (registration to the first image). Motion parameters never exceeded 0.5 mm or 0.4° rotation except in one run of one animal, which was discarded (the animal experienced anesthesia-induced emesis during the last run). Images were slice-time corrected and EPI distortion corrected using *topup*. High magnetic fields and large matrix sizes are commonly associated with severe EPI distortions. Anatomical images were nonlinearly warped into the "National Institute of Mental Health Macaque Template" (NMT) (Seidlitz et al., 2018) template using ANTs and 3DQwarp in AFNI. The distortion correction, motion correction and normalization were performed using a single sinc interpolation. Images were spatially smoothed (FWHM = 2 mm), linear detrended, denoised using a linear regression approach including heart rate and respiration, as well as a 5 component nuisance regressor of the masked white matter and cerebrospinal fluid and band-pass filtering (0.008 - 0.09 Hz) (Hallquist, Hwang, & Luna, 2013).

4.4. INTs

Based on previous studies (Murray et al., 2014; Watanabe et al., 2019), INTs were calculated by estimating the magnitude of the autocorrelation of the preprocessed functional data. At the single-subject level, the INT of each voxel was quantified as follows. For each run, the autocorrelation function (ACF) of each voxel's fMRI signal was estimated. The ACF is the correlation of y_t (time series) and y_{t+k} (lagged time series), where k represents the time lag in steps of TR. Next, the sum of ACF values was calculated in the initial positive period. The upper limit of this period was set at the point where the ACF first becomes negative as the time lag increases. The result was used as an index of the INT of the brain region. At the single-subject level, the number of INT maps was dependent on the number of functional runs. The maps were not smoothed, because individual

variation in FC gradients and INTs has been shown to have functional significance (Przeździk et al., 2019; Watanabe et al., 2019).

To examine the correspondence between fMRI-based and electrophysiology-based INT hierarchies, the values of individual voxels were averaged within areas. The areas were defined based on the Cortical Hierarchy Atlas of the Rhesus Macaque (CHARM) (Jung et al., 2021) and Subcortical Atlas of the Rhesus Macaque (SARM) (Hartig et al., 2021) to closely match the corresponding electrophysiological recording sites (see Supplementary File 1). In some cases, since the CHARM parcellation did not match the recording sites, the regions of interest were drawn.

Since the hemodynamic INTs were estimated as the sum of ACF values in the initial positive period, this measurement considers both the number of lags and the magnitude of the ACF values. As a result, the hemodynamic INTs do not have a time unit and are used as a proxy of the timescale of that area, with higher values reflecting longer timescales. We have additionally provided the estimated time constants associated with the INT hierarchies that have been previously described with electrophysiological recordings by multiplying the 0-crossing lag by the TR (see Figure 1 Supplement 2 for an estimate of the time constants).

Stability and similarity

The intra-subject stability was quantified by calculating the pairwise correlation (i.e., Pearson's r) between the runs. The individual stability score was computed by averaging the Fisher's Z-transformed correlation coefficients across pairwise comparisons. For every subject, the maps were averaged across runs to quantify the inter-subject similarity. The individual similarity score was computed by averaging the subject's Fisher's Z-transformed correlation coefficients with all the other subjects.

To quantify the stability of the hierarchies, they were re-computed for groups of four subjects. The resulting ranking was correlated (i.e., Spearman's Rank correlation) with the group-level ordering of the cortical/subcortical regions. To estimate the stability score, this procedure was repeated for all the possible combinations of subjects (i.e., n = 126). The stability score of any hierarchy was computed by averaging the correlation coefficients across steps (i.e., n = 126).

4.5. FC gradients

We computed FC gradients using BrainSpace, a toolbox for the identification, visualization, and analysis of macroscale gradients in neuroimaging datasets (Vos de Wael et al., 2020).

The input matrix

The input matrix consisted of the voxel-wise FC between or within areas. The Pearson correlation coefficient between the time-series of every pair of voxels within and/or between areas was computed. This resulted in a 2D matrix of correlation coefficients, with every voxel being represented by an n-dimensional row vector (with n reflecting the number of connections). The connectivity matrices were computed for each subject and run.

Generating gradients

The procedure for generating FC gradients was thoroughly described in Vos de Wael et al. (2020). The input matrix was made sparse (10% sparsity) and the cosine similarity kernel was applied to build the affinity matrix. Next, diffusion mapping was applied using the BrainSpace basic parameters. The resulting gradients were plotted on the cortical surface of the NMT template (Seidlitz et al., 2018) using AFNI (Cox, 1996) and SUMA (Ziad S Saad & Reynolds, 2012; Z. S. Saad, Reynolds, Argall, Japee, & Cox, 2004). The gradients were generated bilaterally. We only report the gradient most correlated with the INT map, assuming that ensuing gradients reflect other principles of functional organization.

Cortical projection

To probe the relationship between the striatal FC gradients and the cortex, the striatal FC gradients were projected onto the cortex according to the highest-correlated voxels (Haak et al., 2018). To reduce noise and improve interpretability, the resulting maps were smoothed using AFNI (Cox, 1996).

4.6. Projecting INTs based on FC

To examine the relationship between INTs and FC between areas (e.g., between cortex and striatum), cortical INTs were projected onto a striatal map based on cortico-striatal FC. For every striatal voxel, the top 10 highest functionally correlated cortical voxels were identified. Next, the INTs associated with these cortical voxels were extracted. Finally, the average associated cortical INT value was computed for each striatal voxel and represented as a map.

5. Supplementary files

Hierarchy	Area	Level	Code
Murray et al., 2014	OFC	3	25
	ACC	3	3
	LPFC	2	50
	S1	3	92
	S2	3	95
	LIP	5	115
	MT	5	232
Fascianelli et al. 2019; and Cirillo et al., 2018	PFo	3	25
	DLPFC	6	63, 67, 68
	PFp	Custom	Custom
	PMd	5	81
Cavanagh et al., 2018	DLPFC	6	63, 67, 68
	VLPFC	6	53, 70, 74, 75
	ACC	6	10, 62
Maisson et al., 2021	vmPFC	5	22
	pgACC	6	4
	sgACC	6	5
	dACC	Custom	Custom

Nougaret et al., 2021	Striatum	3	43
	STN	5	91
	GPe	6	56

Supplementary File 1. The areas were defined based on a cortical and subcortical atlas.

The areas in Figure 1 were defined based on the Cortical Hierarchy Atlas of the Rhesus Macaque (CHARM) (Jung et al., 2021) and Subcortical Atlas of the Rhesus Macaque (SARM) (Hartig et al., 2021) to closely match the corresponding electrophysiological recording sites. For some of the cortical regions of interest, the CHARM parcellation did not match the recording sites. As a result, the areas were defined according to the respective descriptions (Note: this is the case whenever "Custom" is indicated in the table). Abbreviations: S1/S2 (primary/secondary somatosensory cortex), MT (middle temporal area), LIP (lateral intraparietal area), OFC (orbitofrontal cortex), LPFC (lateral prefrontal cortex), ACC (anterior cingulate cortex), PMd (dorsal premotor cortex), LOFC (lateral OFC), DLPFC (dorso-lateral PFC), VLPFC (ventro-lateral PFC), PFp (polar prefrontal cortex), vmPFC (ventro-medial PFC), sgACC (subgenual ACC), pgACC (pregenual ACC), dACC (dorsal ACC), GPe (external globus pallidus), STN (subthalamic nucleus).

Hierarchy	**Area**	**Level**	**Code**
Original Dorsal Pathway	V1	3	246
	V2/3	3	237
	PG	6	122
	DLPFC	3	54
Occipito-parietal pathway	V1	3	246
	V2	4	243
	V3	4	238

	V6	4	98
Parieto-premotor pathway	V6A	4	99
	MIP	5	108
	PMd	5	81
	PMv	5	84
	VIP	6	110
	rIPL	6	123
Parieto-prefrontal pathway	MT	6	232
	MST	6	119
	8A	5	51
	46	5	63, 66

Supplementary File 2. Areas defined based on a cortical atlas.

The areas in Figure 2 were defined based on the Cortical Hierarchy Atlas of the Rhesus Macaque (CHARM) (Jung et al., 2021) to match the hierarchies described by Kravitz et al. (2011). Abbreviations: DLPFC (dorso-lateral prefrontal cortex), VIP (ventral intraparietal area), MIP (medial intraparietal area), rIPL (rostral inferior parietal lobule, MT (middle temporal area), MST (medial superior temporal area), LIP (lateral intraparietal area), A46 (area 46), A8A (area 8A), PMd (dorsal premotor cortex), PMv (ventral premotor cortex).

6. References

Autio, J. A., Zhu, Q., Li, X., Glasser, M. F., Schwiedrzik, C. M., Fair, D. A., . . . Vanduffel, W. (2021). Minimal specifications for non-human primate MRI: Challenges in standardizing and harmonizing data collection. Neuroimage, 236, 118082. doi:10.1016/j.neuroimage.2021.118082

Avants, B. B., Tustison, N. J., Stauffer, M., Song, G., Wu, B., & Gee, J. C. (2014). The Insight ToolKit image registration framework. *Frontiers in Neuroinformatics, 8*(44). doi:10.3389/fninf.2014.00044

Avants, B. B., Tustison, N. J., Wu, J., Cook, P. A., & Gee, J. C. (2011). An Open Source Multivariate Framework for n-Tissue Segmentation with Evaluation on Public Data. *Neuroinformatics, 9*(4), 381-400. doi:10.1007/s12021-011-9109-y

Badre, D. (2008). Cognitive control, hierarchy, and the rostro-caudal organization of the frontal lobes. *Trends Cogn Sci, 12*(5), 193-200. doi:10.1016/j.tics.2008.02.004

Binkofski, F., & Buxbaum, L. J. (2013). Two action systems in the human brain. *Brain Lang, 127*(2), 222-229. doi:10.1016/j.bandl.2012.07.007

Carmichael, S. T., & Price, J. L. (1994). Architectonic subdivision of the orbital and medial prefrontal cortex in the macaque monkey. *J Comp Neurol, 346*(3), 366-402. doi:10.1002/cne.903460305

Carmichael, S. T., & Price, J. L. (1996). Connectional networks within the orbital and medial prefrontal cortex of macaque monkeys. *Journal of Comparative Neurology, 371*(2), 179-207. doi:10.1002/(SICI)1096-9861(19960722)371:2<179::AID-CNE1>3.0.CO;2-#

Cavanagh, S. E., Hunt, L. T., & Kennerley, S. W. (2020). A diversity of intrinsic timescales underlie neural computations. *Frontiers in Neural Circuits, 14*, 81.

Cavanagh, S. E., Hunt, L. T., & Kennerley, S. W. (2020). A Diversity of Intrinsic Timescales Underlie Neural Computations. *Frontiers in Neural Circuits, 14*(81). doi:10.3389/fncir.2020.615626

Cavanagh, S. E., Wallis, J. D., Kennerley, S. W., & Hunt, L. T. (2016). Autocorrelation structure at rest predicts value correlates of single neurons during reward-guided choice. *eLife, 5*, e18937. doi:10.7554/eLife.18937

Chaudhuri, R., Knoblauch, K., Gariel, M.-A., Kennedy, H., & Wang, X.-J. (2015). A Large-Scale Circuit Mechanism for Hierarchical Dynamical Processing in the Primate Cortex. *Neuron, 88*(2), 419-431. doi:https://doi.org/10.1016/j.neuron.2015.09.008

Cirillo, R., Fascianelli, V., Ferrucci, L., & Genovesio, A. (2018). Neural Intrinsic Timescales in the Macaque Dorsal Premotor Cortex Predict the Strength of Spatial Response Coding. *iScience, 10*, 203-210. doi:https://doi.org/10.1016/j.isci.2018.11.033

Cox, R. W. (1996). AFNI: Software for Analysis and Visualization of Functional Magnetic Resonance Neuroimages. *Computers and Biomedical Research, 29*(3), 162-173. doi:https://doi.org/10.1006/cbmr.1996.0014

Demirtaş, M., Burt, J. B., Helmer, M., Ji, J. L., Adkinson, B. D., Glasser, M. F., . . . Murray, J. D. (2019). Hierarchical heterogeneity across human cortex shapes large-scale neural dynamics. *Neuron, 101*(6), 1181-1194. e1113.

Fascianelli, V., Tsujimoto, S., Marcos, E., & Genovesio, A. (2019). Autocorrelation Structure in the Macaque Dorsolateral, But not Orbital or Polar, Prefrontal Cortex Predicts Response-Coding Strength in a Visually Cued Strategy Task. *Cereb Cortex, 29*(1), 230-241. doi:10.1093/cercor/bhx321

Gao, R., van den Brink, R. L., Pfeffer, T., & Voytek, B. (2020). Neuronal timescales are functionally dynamic and shaped by cortical microarchitecture. *eLife, 9*, e61277. doi:10.7554/eLife.61277

Goodale, M. A., Meenan, J. P., Bülthoff, H. H., Nicolle, D. A., Murphy, K. J., & Racicot, C. I. (1994). Separate neural pathways for the visual analysis of object shape in perception and prehension. *Current Biology, 4*(7), 604-610.

Goodale, M. A., & Milner, A. D. (1992). Separate visual pathways for perception and action. *Trends in Neurosciences, 15*(1), 20-25.

Grier, M. D., Zimmermann, J., & Heilbronner, S. R. (2020). Estimating Brain Connectivity With Diffusion-Weighted Magnetic Resonance Imaging: Promise and Peril. *Biological Psychiatry: Cognitive Neuroscience and Neuroimaging, 5*(9), 846-854. doi:https://doi.org/10.1016/j.bpsc.2020.04.009

Haak, K. V., & Beckmann, C. F. (2020). Understanding brain organisation in the face of functional heterogeneity and functional multiplicity. *Neuroimage, 220*, 117061. doi:https://doi.org/10.1016/j.neuroimage.2020.117061

Haak, K. V., Marquand, A. F., & Beckmann, C. F. (2018). Connectopic mapping with resting-state fMRI. *Neuroimage, 170*, 83-94. doi:10.1016/j.neuroimage.2017.06.075

Haber, S. N. (2016). Corticostriatal circuitry. *Dialogues Clin Neurosci, 18*(1), 7-21. doi:10.31887/DCNS.2016.18.1/shaber

Haber, S. N., & Knutson, B. (2010). The reward circuit: linking primate anatomy and human imaging. *Neuropsychopharmacology, 35*(1), 4-26. doi:10.1038/npp.2009.129

Hallquist, M. N., Hwang, K., & Luna, B. (2013). The nuisance of nuisance regression: spectral misspecification in a common approach to resting-state fMRI preprocessing reintroduces noise and obscures functional connectivity. *Neuroimage, 82*, 208-225.

Hartig, R., Glen, D., Jung, B., Logothetis, N. K., Paxinos, G., Garza-Villarreal, E. A., . . . Evrard, H. C. (2021). The Subcortical Atlas of the Rhesus Macaque (SARM) for neuroimaging. *Neuroimage, 235*, 117996. doi:https://doi.org/10.1016/j.neuroimage.2021.117996

Hasson, U., Yang, E., Vallines, I., Heeger, D. J., & Rubin, N. (2008). A Hierarchy of Temporal Receptive Windows in Human Cortex. *The Journal of Neuroscience, 28*(10), 2539-2550. doi:10.1523/jneurosci.5487-07.2008

Honey, C. J., Thesen, T., Donner, T. H., Silbert, L. J., Carlson, C. E., Devinsky, O., . . . Hasson, U. (2012). Slow cortical dynamics and the accumulation of information over long timescales. *Neuron, 76*(2), 423-434. doi:10.1016/j.neuron.2012.08.011

Ito, T., Hearne, L. J., & Cole, M. W. (2020). A cortical hierarchy of localized and distributed processes revealed via dissociation of task activations, connectivity changes, and intrinsic timescales. Neuroimage, 221, 117141.

Jbabdi, S., Sotiropoulos, S. N., & Behrens, T. E. (2013). The topographic connectome. *Curr Opin Neurobiol, 23*(2), 207-215. doi:10.1016/j.conb.2012.12.004

Jenkinson, M., Beckmann, C. F., Behrens, T. E. J., Woolrich, M. W., & Smith, S. M. (2012). FSL. *Neuroimage, 62*(2), 782-790. doi:https://doi.org/10.1016/j.neuroimage.2011.09.015

Jung, B., Taylor, P. A., Seidlitz, J., Sponheim, C., Perkins, P., Ungerleider, L. G., . . . Messinger, A. (2021). A comprehensive macaque fMRI pipeline and hierarchical atlas. *Neuroimage, 235*, 117997. doi:https://doi.org/10.1016/j.neuroimage.2021.117997

Kiebel, S. J., Daunizeau, J., & Friston, K. J. (2008). A Hierarchy of Time-Scales and the Brain. *PLOS Computational Biology, 4*(11), e1000209. doi:10.1371/journal.pcbi.1000209

Kravitz, D. J., Saleem, K. S., Baker, C. I., & Mishkin, M. (2011). A new neural framework for visuospatial processing. *Nature Reviews Neuroscience, 12*(4), 217-230. doi:10.1038/nrn3008

Lagore, R. L., Moeller, S., Zimmermann, J., DelaBarre, L., Radder, J., Grant, A., . . . Adriany, G. (2021). An 8-dipole transceive and 24-loop receive array for non-human primate head imaging at 10.5 T. *NMR in Biomedicine, 34*(4), e4472.

Logothetis, N. K., Pauls, J., Augath, M., Trinath, T., & Oeltermann, A. (2001). Neurophysiological investigation of the basis of the fMRI signal. *nature, 412*(6843), 150-157.

Maisson, D. J. N., Cash-Padgett, T. V., Wang, M. Z., Hayden, B. Y., Heilbronner, S. R., & Zimmermann, J. (2021). Choice-relevant information transformation along a ventrodorsal axis in the medial prefrontal cortex. *Nature Communications, 12*(1), 4830. doi:10.1038/s41467-021-25219-w

Marquand, A. F., Haak, K. V., & Beckmann, C. F. (2017). Functional corticostriatal connection topographies predict goal-directed behaviour in humans. *Nature Human Behaviour, 1*(8), 0146. doi:10.1038/s41562-017-0146

Moeller, S., Yacoub, E., Olman, C. A., Auerbach, E., Strupp, J., Harel, N., & Uğurbil, K. (2010). Multiband multislice GE-EPI at 7 tesla, with 16-fold acceleration using partial parallel imaging with application to high spatial and temporal whole-brain fMRI. *Magnetic Resonance in Medicine, 63*(5), 1144-1153.

Murray, J. D., Bernacchia, A., Freedman, D. J., Romo, R., Wallis, J. D., Cai, X., . . . Wang, X.-J. (2014). A hierarchy of intrinsic timescales across primate cortex. *Nature neuroscience, 17*(12), 1661-1663. doi:10.1038/nn.3862

Nougaret, S., Fascianelli, V., Ravel, S., & Genovesio, A. (2021). Intrinsic Timescales Across the Basal Ganglia. *bioRxiv*, 2021.2004.2007.438040. doi:10.1101/2021.04.07.438040

Ogawa, T., & Komatsu, H. (2010). Differential temporal storage capacity in the baseline activity of neurons in macaque frontal eye field and area V4. *J Neurophysiol, 103*(5), 2433-2445. doi:10.1152/jn.01066.2009

Öngür, D., & Price, J. L. (2000). The Organization of Networks within the Orbital and Medial Prefrontal Cortex of Rats, Monkeys and Humans. *Cerebral Cortex, 10*(3), 206-219. doi:10.1093/cercor/10.3.206

Price, J. L. (1999). Networks within the orbital and medial prefrontal cortex. *Neurocase, 5*(3), 231-241. doi:10.1080/13554799908402728

Przeździk, I., Faber, M., Fernández, G., Beckmann, C. F., & Haak, K. V. (2019). The functional organisation of the hippocampus along its long axis is gradual and predicts recollection. *Cortex, 119*, 324-335. doi:https://doi.org/10.1016/j.cortex.2019.04.015

Raut, R. V., Snyder, A. Z., & Raichle, M. E. (2020). Hierarchical dynamics as a macroscopic organizing principle of the human brain. *Proceedings of the National Academy of Sciences, 117*(34), 20890-20897. doi:10.1073/pnas.2003383117

Riley, M. R., Qi, X.-L., Zhou, X., & Constantinidis, C. (2018). Anterior-posterior gradient of plasticity in primate prefrontal cortex. *Nature Communications, 9*(1), 3790. doi:10.1038/s41467-018-06226-w

Rossi-Pool, R., Zainos, A., Alvarez, M., Parra, S., Zizumbo, J., & Romo, R. (2021). Invariant timescale hierarchy across the cortical somatosensory network. *Proceedings of the National Academy of Sciences, 118*(3), e2021843118. doi:10.1073/pnas.2021843118

Saad, Z. S., & Reynolds, R. C. (2012). Suma. *Neuroimage, 62*(2), 768-773.

Saad, Z. S., Reynolds, R. C., Argall, B., Japee, S., & Cox, R. W. (2004, 18-18 April 2004). *SUMA: an interface for surface-based intra- and inter-subject analysis with AFNI.*

Paper presented at the 2004 2nd IEEE International Symposium on Biomedical Imaging: Nano to Macro (IEEE Cat No. 04EX821).

Seidlitz, J., Sponheim, C., Glen, D., Ye, F. Q., Saleem, K. S., Leopold, D. A., . . . Messinger, A. (2018). A population MRI brain template and analysis tools for the macaque. *Neuroimage, 170*, 121-131. doi:10.1016/j.neuroimage.2017.04.063

Setsompop, K., Gagoski, B. A., Polimeni, J. R., Witzel, T., Wedeen, V. J., & Wald, L. L. (2012). Blipped-controlled aliasing in parallel imaging for simultaneous multislice echo planar imaging with reduced g-factor penalty. *Magnetic Resonance in Medicine, 67*(5), 1210-1224.

Shinn, M., Hu, A., Turner, L., Noble, S., Achard, S., Anticevic, A., . . . Bullmore, E. T. (2021). Spatial and temporal autocorrelation weave human brain networks. bioRxiv.

Soltani, A., Murray, J. D., Seo, H., & Lee, D. (2021). Timescales of cognition in the brain. *Current Opinion in Behavioral Sciences, 41*, 30-37. doi:https://doi.org/10.1016/j.cobeha.2021.03.003

Tan, P. K., Tang, C., Herikstad, R., Pillay, A., & Libedinsky, C. (2020). Distinct lateral prefrontal regions are organized in an anterior-posterior functional gradient. *bioRxiv*, 2020.2012.2016.423034. doi:10.1101/2020.12.16.423034

Uğurbil, K., Xu, J., Auerbach, E. J., Moeller, S., Vu, A. T., Duarte-Carvajalino, J. M., . . . Van de Moortele, P. F. (2013). Pushing spatial and temporal resolution for functional and diffusion MRI in the Human Connectome Project. *Neuroimage, 80*, 80-104.

Ugurbil, K. (2016). What is feasible with imaging human brain function and connectivity using functional magnetic resonance imaging. Philosophical Transactions of the Royal Society B: Biological Sciences, 371(1705), 20150361.

Uğurbil, K. (2018). Imaging at ultrahigh magnetic fields: History, challenges, and solutions. Neuroimage, 168, 7-32.

Uğurbil, K., Auerbach, E., Moeller, S., Grant, A., Wu, X., Van de Moortele, P. F., . . . Radder, J. (2019). Brain imaging with improved acceleration and SNR at 7 Tesla obtained with 64-channel receive array. Magnetic Resonance in Medicine, 82(1), 495-509.

Vos de Wael, R., Benkarim, O., Paquola, C., Lariviere, S., Royer, J., Tavakol, S., . . . Bernhardt, B. C. (2020). BrainSpace: a toolbox for the analysis of macroscale gradients in neuroimaging and connectomics datasets. *Communications Biology, 3*(1), 103. doi:10.1038/s42003-020-0794-7

Watanabe, T., Rees, G., & Masuda, N. (2019). Atypical intrinsic neural timescale in autism. *eLife, 8*, e42256. doi:10.7554/eLife.42256

Wengler, K., Goldberg, A., Chahine, G., & Horga, G. (2020). *Distinct Hierarchical Alterations of Intrinsic Neural Timescales Account for Different Manifestations of Psychosis*.

Whitfield-Gabrieli, S., & Nieto-Castanon, A. (2012). Conn: a functional connectivity toolbox for correlated and anticorrelated brain networks. *Brain Connect, 2*(3), 125-141. doi:10.1089/brain.2012.0073

Wong, A. L., Haith, A. M., & Krakauer, J. W. (2015). Motor Planning. *The Neuroscientist, 21*(4), 385-398. doi:10.1177/1073858414541484

Yacoub, E., Grier, M. D., Auerbach, E. J., Lagore, R. L., Harel, N., Adriany, G., . . . Zimmermann, J. (2020). Ultra-high field (10.5 T) resting state fMRI in the macaque. *Neuroimage, 223*, 117349. doi:https://doi.org/10.1016/j.neuroimage.2020.117349

Zilio, F., Gomez-Pilar, J., Cao, S., Zhang, J., Zang, D., Qi, Z., . . . Northoff, G. (2021). Are intrinsic neural timescales related to sensory processing? Evidence from abnormal behavioral states. *Neuroimage, 226*, 117579. doi:https://doi.org/10.1016/j.neuroimage.2020.117579

Zimmermann, J., Glimcher, P. W., & Louie, K. (2018). Multiple timescales of normalized value coding underlie adaptive choice behavior. *Nature Communications, 9*(1), 3206. doi:10.1038/s41467-018-05507-8